NTNU – Trondheim
Norwegian University of
Science and Technology

Nucleation of Primary Mg_2Si in Al-Mg-Si Alloys

Torstein Grøstad

Materials Science and Engineering
Submission date: June 2014
Supervisor: Lars Arnberg, IMTE
Co-supervisor: Thomas Ludwig, Hydro Aluminium AS Årdal

Norwegian University of Science and Technology
Department of Materials Science and Engineering

Preface

This thesis is submitted as a partial fulfillment of the requirements for the degree of Master of Science (MSc) in Materials Science and Engineering at Norwegian University of Science and Technology. The work presented in the master thesis is a result of the work during the spring term, and is not a continuation of a project work during the autumn term of 2013. The findings in the thesis are to be submitted for publication in Journal of Alloys and Compounds under the title: "*Effect of P addition on primary Mg_2Si in a high purity Al-15Mg_2Si-5Si alloy*".

I hereby declare that the work presented in this master thesis has been performed independently and in accordance with the rules and regulations of the Norwegian University of Science and Technology (NTNU).

Trondheim, June 13, 2014

Torstein Grøstad

Abstract

Al-Mg_2Si Metal Matrix Composites have the potential to replace the frequently used near- and hyper-eutectic Al-Si alloys. In the as-cast condition, these alloys can contain coarse dendritic primary Mg_2Si particles which have adverse effects on the mechanical properties. The effects of P additions on the primary Mg_2Si particles and the eutectic structures in an Al-15Mg_2Si-5Si alloy were investigated by thermal analysis and microstructural examination. Test alloys with nominal phosphorous contents of 0, 5, 20, 40, 60, 80, 100 and 500 ppm P were prepared. Confirmative composition measurements were carried out by glow discharge mass spectrometry (GDMS). With increasing P addition the primary Mg_2Si particles were considerably refined, and the morphology changed from coarse dendritic to fine polygonal particles. Thermal analysis revealed that the nucleation temperature for primary Mg_2Si increased from 640.6 °C to 651.2 °C with addition of 5 ppm P, and reached a maximum of 656.4 °C with addition of 20 ppm P. AlP particles were confirmed to act as nuclei for primary Mg_2Si particles by chemical analysis in an Electron Probe Micro Analyzer (EPMA). It is argued that for P additions up to 60 ppm, nucleation occurs on *all* favorable AlP particles, leading to site saturation. For higher P contents, it is suggested that the recalescence reduces the initial growth rate, allowing the formation of an Al-enriched boundary layer around the growing crystal. This retards further growth in all directions, causing the morphology change from dendritic to polygonal.

Sammendrag

Al-Mg_2Si metall-matriks kompositter har potensiale til å erstatte de mye brukte nær- og hyper-eutektiske Al-Si legeringene. I støpt tilstand kan disse legeringene inneholde grove primære Mg_2Si dendritter, som har negative effekter på de mekaniske egenskapene. Effektene av ulike P tilsatser på de primære Mg_2Si partiklene samt de eutektiske strukturene i en Al-15Mg_2Si-5Si legering ble studert med termisk analyse og mikrostrukturelle undersøkelser. Testlegeringer med nominelt fosforinnhold på 0, 5, 20, 40, 60, 80, 100 og 500 ppm ble tillaget. Bekreftende kjemiske analyser ble utført med *glow discharge mass spectrometry* (GDMS). De primære Mg_2Si partiklene ble betydelig forfinet med økende P tilsats, og morfologien ble endret fra grove dendritter til fine polygonale partikler. Termiske analyser viste at kimdanningstemperaturen for primært Mg_2Si økte fra 640.6 °C til 651.2 °C med tilsats av 5 ppm P, og nådde et maksimum på 656.4 °C ved tilsats av 20 ppm P. AlP partikler ble bekreftet som kimdannere for primære Mg_2Si partikler ved kjemiske analyser i mikrosonde. Det er argumentert for at kimdanning skjer på *alle* gunstige AlP partikler for P tilsatser opp til 60 ppm og at vi dermed har *site saturation*. For høyere P tilsatser, foreslås det at rekalescensen reduserer den initielle veksthastigheten og dermed tillater dannelsen av et grensesjikt rikt på Al omkring den voksende krystallen. Dette grensesjiktet bremser videre vekst i alle retninger, og forårsaker morfologiendringen fra dendrittisk til polygonal.

Table of Contents

1 Introduction

The last decades Metal-Matrix Composites (MMCs) have gained increasing interest, particularly in the automotive and aerospace industry. These industries are driven towards lighter weight and increased material quality to meet the growing demands for lower emissions and better fuel efficiency. Al based MMCs have the potential to replace near-eutectic and hyper-eutectic Al-Si alloys which are very much used in the automotive industry. Applications for these materials include parts such as cylinder heads, piston rods (Figure 1) and brake disks (Figure 2). Al-Mg_2Si MMCs have a large potential for wear-resistant applications, as the intermetallic compound Mg_2Si has a high melting temperature (1085 °C), low density (1.99 g · cm^{-3}), low thermal expansion coefficient (7.5 · 10^{-6} K^{-1}), high hardness and an elastic modulus of 120 GPa [1].

Figure 1: MMC piston rods. Courtesy of MX Composites [2].

Figure 2: MMC brake disks. Courtesy of REL, Inc [3].

If MMCs are to gain a large industrial viability, the processing must be economical and reliable. A large part of existing MMCs are prepared by ex situ processes through several process steps. In addition to being expensive, these processes possess some challenges such as poor wetting of the reinforcement, reaction of the matrix-reinforcement interface, segregation and large particle sizes [4]. In situ preparation of such alloys are therefore of large interest, as fewer production steps reduce cost. Moreover, the reinforcing particles precipitate during solidification, leading to better wetting of the reinforcement.

As-cast in situ Al-Mg_2Si MMCs often have poor mechanical properties due to coarse dendritic primary Mg_2Si particles. These particles need to be modified in order to ensure good mechanical properties. In the present work, the term modification refers to a

change in the morphology of the primary Mg_2Si particles. The first attempts on modification on the Al-Si system was performed by Pacz in 1921, by adding Na to the melt [5]. Numerous studies have been carried out on modification and refinement of the in situ MMC microstructures. Modification can be achieved by addition of e.g. rare-earth metals [6], K_2TiF_6 [7], Li [8], Na [9], P [10], Sb [11] or Sr [12]. In addition, the mechanical properties can be improved by more advanced processing such as hot extrusion [13], rapid solidification [14], mechanical alloying [15] and heat treatment after casting [1]. However, these advanced processing techniques are not extensively used in the industry, as they are expensive and the quality is unreliable on an industrial production scale.

The modification effect of phosphorous on primary Mg_2Si particles is well established. There are various methods of adding phosphorous; most commonly is through the addition of a master alloy such as Al-P or Al-Cu-P. The effect is very stable with respect to holding time and causes little gas pollution [16]. Phosphorous modifies the structure by forming AlP particles which act as heterogeneous nucleation sites for primary Mg_2Si. Much of the early work on the modification effect of P deals with Al-Si alloys. Hekmat-Ardakan and Ajersch argued that the growth modes of Si and Mg_2Si are very similar, and thus that the early research on Al-Si alloys also applies to Al-Mg_2Si alloys [17]. This is further supported by the work of Zhang et al. who argued that the binary Al-Si and quasi-ternary Al-Mg_2Si systems are very similar for the case of a hypereutectic alloy, as the growth modes in both cases are characterized by a faceted primary phase, and a faceted and non-faceted phase in the eutectic [6].

Most of the previous work on phosphorous modification has studied phosphorous contents in the range of 0.1 to 1.0 wt %. According to the work by Ludwig et al. on trace element concentrations of P in Al-Si alloys [18], it is expected that P will have an effect on Al-Mg_2Si alloys already at concentrations of a few parts per million (ppm). Concentrations in ppm are given by weight for the remainder of this work unless otherwise is specified. In the coming years, production from recycled aluminium will increase. It is therefore crucial to understand how impurities, even at trace element concentrations, influence the microstructure and properties of the produced alloys.

The aim for this work was to provide temperature measurements and metallographic investigations to determine the effect of phosphorous contents in the range from 5 to

500 ppm to Al-15Mg_2Si-5Si alloys. The level of phosphorous necessary to modify primary Mg_2Si was investigated by thermal analysis, microstructural studies and chemical analysis. The obtained results provide insight as to how trace element concentrations of phosphorous affects Al-Mg_2Si MMCs, which is important in developing these alloys. This work is based on careful composition measurements by glow discharge mass spectrometry (GDMS).

2 Theoretical background

2.1 The Al-Mg_2Si system

The (Al-15Mg_2Si)-Si vertical section, from the position indicated in the ternary Al-Mg-Si phase diagram in Figure 3, is shown in Figure 4. It shows how the solidification path depends on the Si content. In the present work Al-15Mg_2Si-5Si alloys are prepared, and the composition is indicated by the dotted line in Figure 4. During solidification, three main reactions can be identified: Precipitation of primary Mg_2Si (Reaction 1), the Al-Mg_2Si binary eutectic reaction (Reaction 2) and the Al-Mg_2Si-Si ternary eutectic reaction (Reaction 3).

$$L \rightarrow Mg_2Si_P + L_1 \qquad \textit{(Rx. 1.)}$$

$$L_1 + Mg_2Si_P \rightarrow L_2 + \left(Mg_2Si + Al\right)_E + Mg_2Si_P \qquad \textit{(Rx. 2.)}$$

$$L_2 + \left(Mg_2Si + Al\right)_E + Mg_2Si_P \rightarrow \left(Mg_2Si + Al + Si\right)_E + \left(Mg_2Si + Al\right)_E + Mg_2Si_P \qquad \textit{(Rx. 3.)}$$

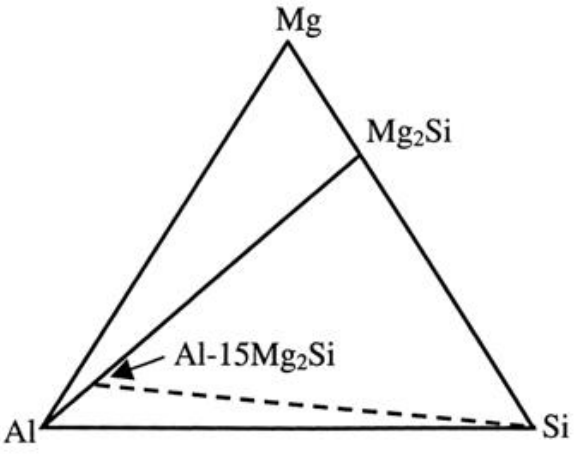

Figure 3: Schematic illustration of the position of the vertical section in the ternary Al-Mg-Si phase diagram. The dotted line indicates the position of the pseudo-binary (Al-15Mg_2Si)-Si system shown in Figure 4. Adapted from Figure 2 [19].

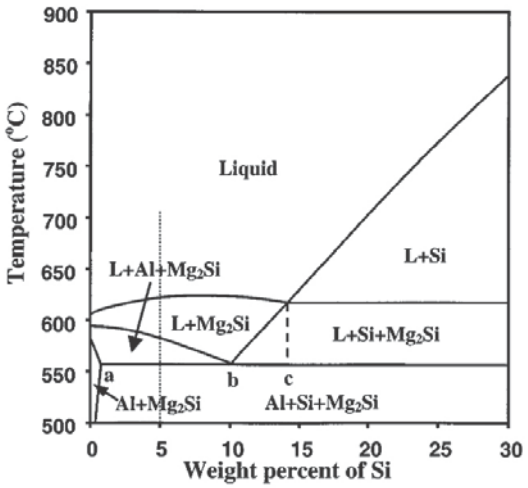

Figure 4: Vertical section of the ternary Al-Mg-Si phase diagram showing the quasi-binary (Al-15Mg_2Si)-Si phase diagram. The alloy composition in the present work is indicated by the dotted line. Adapted from Figure 3 [19].

2.2 Nucleation theory

Homogeneous nucleation

Before a solid phase can grow from the melt, it is necessary that atomic clusters of the phase already exists. Due to thermal fluctuations in the melt these small atomic clusters or embryos can form even above the melting point. These will remain metastable below the melting point due to the large energy required to create the solid-liquid interface [20, p. 22]. This implies that nucleation always will require some degree of undercooling.

A spherical embryo with radius r is assumed and the standard Gibbs free energy of formation can be expressed by Equation 1.

$$\Delta G = -\frac{4}{3}\pi r^3 \Delta G_v + 4\pi r^2 \sigma \qquad \textit{(Eq. 1.)}$$

where ΔG_v is the Gibbs energy per unit volume and σ is the specific surface free energy of the interface between the embryo and the melt.

When ΔG_v is positive, ΔG will have a maximum value at a critical size r^*, as shown in Figure 5, given by Equation 2.

$$r^* = \frac{2\sigma}{\Delta G_v} \qquad \textit{(Eq. 2.)}$$

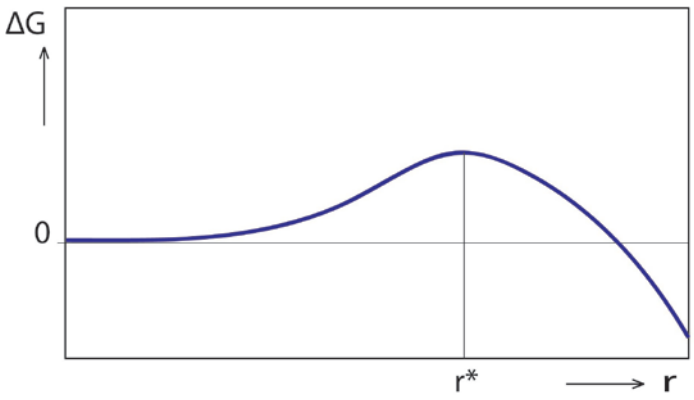

Figure 5: Schematic drawing of the variation of the Gibbs free energy with radius of the embryo for the case of homogeneous nucleation. Adapted from Figure 2.2c [20, p. 25].

The assumption of a spherical embryo implies an isotropic surface energy σ and the configuration with the lowest surface area, thus the lowest resistance to nucleation for a given volume. This is considered a reasonable assumption for most common metals [21].

Due to the random attachment and detachment of atoms to the embryo the size will vary. It is first when the radius exceeds r^* that stable growth will occur due to the resulting decrease in Gibbs free energy [20, p. 25]. In practice, homogeneous nucleation does not occur due to the large undercoolings required (typically > 20 % of the absolute melting point). Therefore, nucleation is considered to occur heterogeneously for industrial solidification processes [22].

Heterogeneous nucleation

Nucleation on pre-existing surfaces allows for nuclei with larger radius and smaller interfacial energy. The main aim of a substrate is to reduce the barrier for nucleation by reducing the energy required for surface formation. This is achieved by replacing some of the high energy solid-liquid interface with a lower energy solid-particle interface [20, pp. 27-28]. This can be seen schematically in Figure 6.

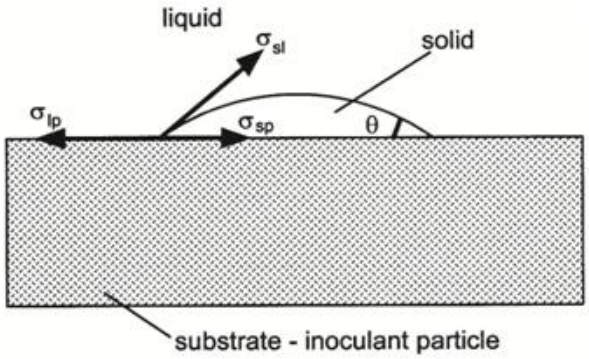

Figure 6: Heterogeneous nucleation from the liquid melt on a flat substrate or inoculant particle. The nucleus has a contact angle θ with the substrate. σ_{sl}, σ_{lp} and σ_{sp} are the surface energies of the solid-liquid, liquid-particle and solid-particle interfaces respectively. Adapted from Figure 13.2 [22].

The contact angle θ is determined by the difference between the surface energy of the liquid-particle interface, the solid-liquid interface and the solid-particle interface. Based on geometrical considerations the energy barrier against nucleation will be reduced by a factor $f(\theta)$ given in Equation 3.

$$f(\theta) = \frac{(2+\cos\theta)(1-\cos\theta)^2}{4} \qquad \textit{(Eq. 3.)}$$

For good substrates, giving low contact angles, Gibbs free energy and the number of atoms needed to create a stable nucleus are much lower than for the case of homogeneous nucleation. With less atoms needed to form a stable nucleus, the probability of a nucleation event increases dramatically. This leads to a large increase in the nucleation rate [20, p. 28]. Reliable quantitative modeling of the heterogeneous nucleation rate has shown to be difficult, as even if the nucleating substrates and size distributions are identified, the surface energies and contact angles are unknown. The nucleation rate is proportional to the number of atoms in contact with a unit area of substrate surface, and the substrate size determines the probability of a nucleation event. For most cases, nucleation is followed by rapid growth into the undercooled melt, so that one substrate particle can only support one nucleation event [22].

For the case of heterogeneous nucleation of primary Mg_2Si on AlP particles, the number and size distribution of substrate particles will vary with the concentration of phosphorous in the melt. For a low concentration of phosphorous, the number of particles will be limited. This can lead to site saturation, where nucleation has already occurred on all favorable particles, and solidification proceeds only by further growth of the existing nuclei [22].

Based on the model by Maxwell and Hellawell [23], where it is suggested that the recalescence caused by the first nucleated and growing crystals would suppress further nucleation events, Greer et al. developed a new model for inoculation of aluminium by Al-Ti-B [24]. The basis for this model is transferrable to the case of AlP heterogeneously nucleating Mg_2Si. Greer et al. argued that heterogeneous nucleation itself is not rate controlling for early crystal growth. Instead, they suggested that free growth of a crystal starts at a critical undercooling inversely proportional to the substrate diameter. This model requires the particle size to be treated as a size distribution, rather than a single particle size, as a single particle size would imply that nucleation occurs on all particles simultaneously.

Greer et al. used a substrate with a planar circular facet of diameter d for their calculations, and assumed that nucleation occurs by adsorption of atom layers forming a low contact angle spherical cap. In the early stages of growth the crystal can grow laterally, but when it covers the whole substrate surface it can only grow further by reducing the radius of curvature. The radius approaches a minimum critical radius r^*

where $r^* = d/2$ as shown in Figure 7. By applying the Gibbs-Thomson undercooling [20, pp. 13-14] they related the undercooling necessary for free growth (ΔT_{fg}) to the particle diameter (d) by Equation 4 [24].

$$\Delta T_{fg} = \frac{4\sigma}{\Delta S_v d} \qquad \textit{(Eq. 4.)}$$

where σ is the solid-liquid surface energy, ΔS_v is the entropy of fusion per unit volume and d is the substrate surface diameter.

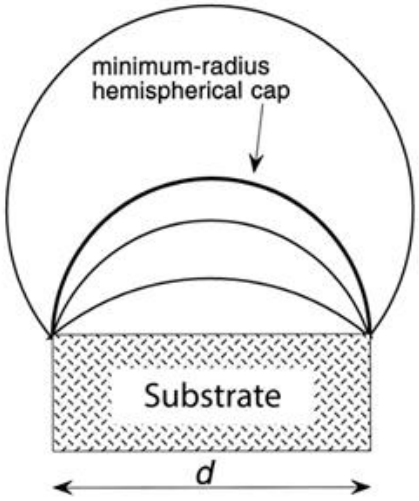

Figure 7: Crystal growth after heterogeneous nucleation on a substrate as described by the free growth model of Greer et al. After covering the substrate surface, the crystal can only grow further by reducing its radius of curvature. The radius approaches a minimum for $r^* = d/2$, where further growth results in an increased radius of curvature and thus decreased Gibbs free energy. The undercooling required for a crystal of radius r^* is defined as the undercooling necessary for free growth (ΔT_{fg}). The figure is adapted from Fig. 1 [24].

2.3 Mechanical properties of Metal-Matrix Composites

Metal-Matrix Composites have gained increasing interest for applications requiring high specific strength, high wear resistance and low thermal expansion. The desirable mechanical properties of Al-Mg_2Si MMCs arise from the combination of relatively hard particles (Mg_2Si) embedded in a ductile matrix (Al). Mg_2Si has favorable properties as a reinforcing particle with high melting temperature (1085 °C), low density (1.99 g · cm^{-3}), low thermal expansion coefficient (7.5 · 10^{-6} K^{-1}), high hardness and an elastic modulus of 120 GPa [1].

Unmodified in situ Al-Mg_2Si MMCs usually exhibit poor ductility due to coarse dendritic Mg_2Si particles. It is established that Mg_2Si particles provide sites for fracture initiation by particle fracture. A fine dispersion of Mg_2Si particles reduces local stress concentrations and thus also the tendency for particle fracture, significantly increasing the ductility [25]. Zhang et al. found that a smaller primary particle size led to a slight increase in the ultimate tensile strength (UTS). As the particle size was too large to contribute to micromechanical strengthening mechanisms such as Orowan strengthening, even in the modified alloys, the factors found to significantly affect the UTS were the matrix grain size and the difference in thermal expansivity between the matrix and the reinforcing particles [26].

Miller and Humphreys discussed these two factors for the case of an Al-SiC MMC. The difference in thermal expansion between aluminum and the reinforcing particles leads to the generation of dislocations when cooling to room temperature after solidification. The Al grain size in MMCs (typically 1 – 10 μm) is significantly finer than what is found in unreinforced alloys and can contribute to strength according to the Hall-Petch equation [27].

2.4 Morphology and growth mechanisms of Mg_2Si

Although it has been established that the morphology of primary Mg_2Si can be changed through alloying or by changing the cooling rate, the exact growth mechanisms have only recently been thoroughly investigated. Li et al. provided a coupled theoretical and experimental analysis of the various morphologies observed in an Al-15Mg_2Si alloy. They found that primary Mg_2Si can possess various morphologies such as faceted octahedron, hopper crystal, truncated octahedron and dendritic, as shown in Figure 8 [28].

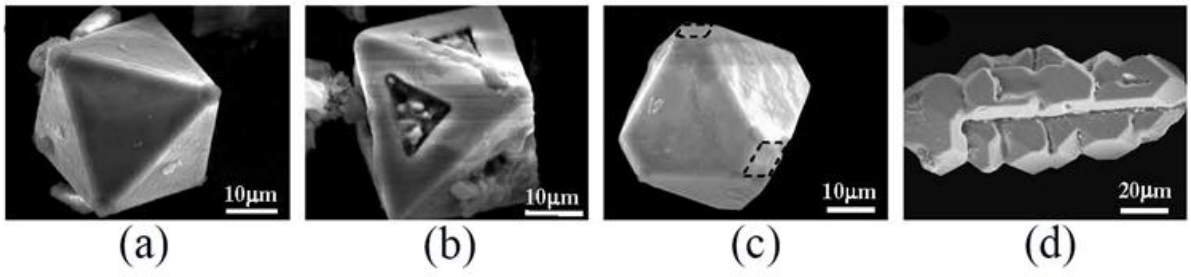

Figure 8: Different morphologies of primary Mg_2Si in Al-15Mg_2Si; (a) faceted octahedron, (b) hopper crystal, (c) truncated octahedron and (d) dendrite. This figure is adapted from Fig. 1 [28].

The final morphology of a crystal is determined by the crystal structure and the crystal growth conditions [29, pp. 60-85]. Thus, if a given crystal such as Mg_2Si varies in morphology it is implied that there is a change in the growth conditions of the crystal.

During crystal growth, new atoms are attached to the crystal surface. The planes with high binding energy tend to grow faster than those with low binding energy. Thus, the low binding energy planes are expected to determine the shape of the crystal. Li et al. found that for the case of Mg_2Si, the {100} planes has the highest growth rate, followed by {110} and {111}. This leads to the octahedral equilibrium shape bounded by eight {111} planes [28].

Following this analysis, a growth mechanism was suggested, and is shown in Figure 9. As the initial growth of the crystal is diffusion controlled, it was suggested that the solute gradient is symmetrical around the embryo. When exceeding a critical size, the solid-liquid interface will become unstable. Small perturbations on the interface will evolve into rapidly growing arms in the preferential <100> directions. The growth of these arms will be limited by the undercooling in the melt. Further growth along the <110> directions from the <100> arms will lead to an octahedral skeleton with symmetric hollows in the centre of the bounding {111} planes. As growth continues in the <111> directions, these hollows become smaller and eventually disappear, leaving a perfectly octahedral Mg_2Si crystal [28].

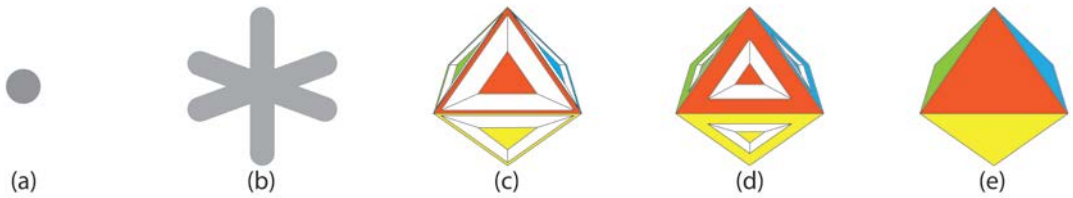

Figure 9: Growth mechanism of octahedral Mg_2Si. (a) Initial symmetrical growth of the embryo. (b) Instability of the solid-liquid interface leading to preferential growth along the six <100> directions. (c) Growth of the <100> arms become limited by the undercooling and growth proceeds successively along the <110> and <111> directions. (d) The hollows at the {111} face centers become smaller and eventually disappear, leaving an octahedral crystal (e). The figure is adapted from Figure 5 [28].

This theoretical analysis is based on a pure Al-Mg_2Si melt. In practice, the growth rate of the crystallographic planes can be altered by changes in the growth conditions such as melt flow, concentration gradients and impurities. Several studies [11, 12, 30] have shown that impurities can greatly affect the growth rate of crystallographic planes.

Impurities can selectively adsorb on particular planes, causing a change in surface energy which alters the growth rate. In addition, impurities can attach onto a growth step during faceted growth and induce growth by twinning (impurity induced twinning) [31]. The melt will be enriched in Al and impurities in front of the growing crystals. The face centers of the {111} planes will experience the largest accumulation. This leads to an increase in constitutional undercooling and decreased growth rate at the face centers, leading to the formation of hopper crystals as shown in Figure 8 (b).

The truncated octahedral morphology, shown in Figure 8 (c), arises from retardation of growth in the <100> directions. This can be caused by impurities adsorbed on the growing planes or limited mass transfer. The different <100> directions can experience different growth conditions as they are at different positions in the melt. This justifies that some of the corners of an octahedron can be truncated, while the rest is not.

2.5 Modification of Mg_2Si

Modification mechanisms

In the present work the term modification refers to a change in the morphology of Mg_2Si. It is important to distinguish between refinement and modification, as a refinement is only a reduction in size of the particles. In many cast alloys, both modification and refinement is wanted, as smaller and more homogenously dispersed equiaxed particles give improved mechanical properties. Modification of primary Mg_2Si can occur by several processes: (i) Addition of substrate-particle-forming elements that act as favorable heterogeneous nucleation sites, where the most common example is AlP; (ii) addition of elements such as Sr and rare earth (RE) metals in small concentrations that induce morphological transformation by adsorbing on preferred crystal planes or accumulating in front of the growing crystal and retarding the growth rate of the crystals in these directions; (iii) or by increasing the cooling rate to restrict the time for diffusion controlled growth [18, pp. 13-14].

Effect of phosphorous addition

Several studies have shown the modification effects of phosphorous additions in hypereutectic Al-Mg_2Si alloys [1, 32, 33]. It is widely accepted that phosphorous modifies primary Mg_2Si by providing heterogeneous nucleation sites in the form of AlP particles. A low disregistry value, or lattice mismatch, between AlP and Mg_2Si facilitate

heterogeneous nucleation. AlP and Mg_2Si have crystal structures and lattice parameters cubic F43m; 5.421 Å and cubic Fd3m; 6.35 Å respectively [1]. For phases with equal atomic arrangements the disregistry value (δ) can be calculated by an equation by Turnbull and Vonnegut [34]. The disregistry value between the {100} planes in AlP and Mg_2Si is 14.6 % which is higher than what is expected for an effective substrate. However, there are other crystallographic planes oriented in such a way that the disregistry value is lower, and a coherent interface is possible as demonstrated by Li et al. [35, 36].

Phosphorous can be present in the bauxite, anodes, recycled scrap or be added in the form of master alloys such as Al-P, Cu-P or Al-Cu-P. Depending on the source of phosphorous the characteristics of the AlP particles will vary. The efficiency of phosphorous additions through master alloys has shown to be the highest as AlP particles are already present in the master alloy [37]. AlP particles exist in three main morphologies depending on the processing route of the master alloy; blocky, dendritic or flaky. These particles are not stable in the melt, and the morphology changes depending on melt temperature and holding time [37].

Qin et al. studied the behavior of AlP particles in Al-Si melts after addition of a master alloy such as Al-Cu-P or Cu-P [38]. They suggested that the process of AlP dissolution proceeded through the following steps:

1. Dissolution of Al_4P tetrahedral units from the larger crystals in the master alloy
2. Formation of the more stable Al_6P unit by addition of two Al atoms from the melt
3. Clustering of Al_6P units in the melt and the formation of $(Al_6P)_n$ micro crystals

This dissolution and clustering process implies that a certain incubation time is necessary for the modification effect by phosphorous addition. This is further supported by the work by Hou et al. who found that a holding time of at least 10 minutes was required to obtain a stable modification effect [16]. As this process continuously approaches dynamic equilibrium, it is very stable even after remelting or overheating [38].

There has been considerable debate over the solubility of phosphorous in aluminium. The recent model presented by Liang and Schmid-Fetzer [39] shows excellent agreement with the experimental data obtained by Lescuyer et al. [40], and is expected

to replace the previous models. According to the model by Liang and Schmid-Fetzer the solubility of phosphorous in liquid Al is 34 ppm at the melting point of aluminium (660.3 °C). There is a drastic solubility drop to 0.07 ppm P in solid Al [39]. In their most recent work, Liang and Schmid-Fetzer developed a self-consistent thermodynamic description of the Al-Si-P ternary system. They used this to develop the first consistent Al-Si-P ternary phase diagram supported by experimental data [41].

The binary Al-P phase diagram is shown in Figure 10, with Figure 11 showing a comparison of the previous models for solubility of P in liquid Al with the recent model by Liang and Schmid-Fetzer. This would suggest that phosphorous would be in solution in liquid Al for concentrations up to 34 ppm P. However, Lescuyer et al. investigated the thermal stability of the preexisting AlP particles from the master alloy at 800 °C, and found that while 60 % of the particles dissolve within 10 minutes after addition, further dissolution proceeds slowly and even 20 hours is not enough to reach equilibrium [40]. Therefore, the amount of dissolved phosphorous in the melt is expected to be well below the solubility limit.

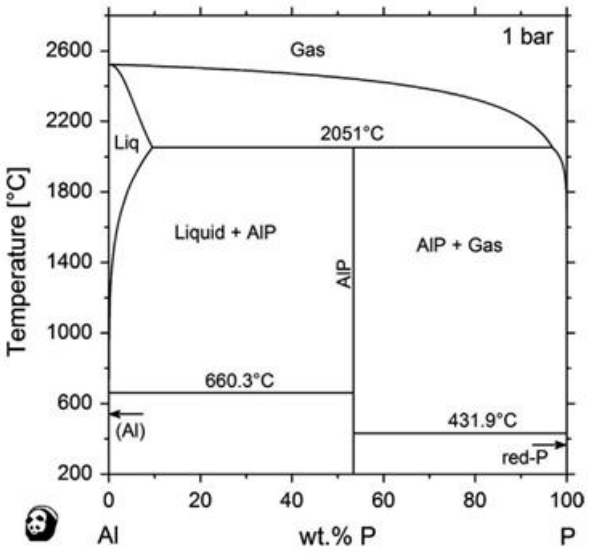

Figure 10: Al-P phase diagram at 1 bar as calculated by Liang and Schmid-Fetzer. Adapted from Fig. 4 [39].

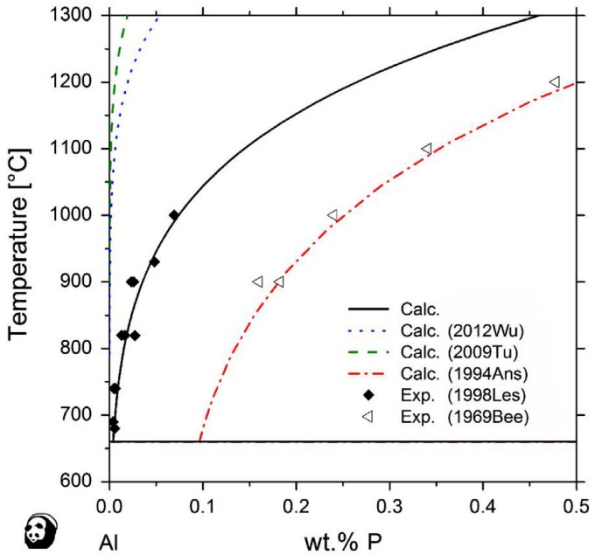

Figure 11: Comparison of different theoretical models with experimental datasets for the solubility of P in liquid Al. The black solid line represents the work of Liang and Schmid-Fetzer, whilst the other datasets referenced are 2012Wu [42], 2009Tu [43], 1994Ans [44], 1998Les [40] and 1969Bee [45]. Adapted from Fig. 2 [39].

3 Experimental work

3.1 Preparation of test alloys

The Al-15Mg_2Si-5Si test alloys were prepared from Al5N-Grade aluminum, Solar Grade (SoG) silicon and high purity magnesium (>99.99 wt%) in boron nitride coated graphite crucibles in a Nabertherm K2 resistance furnace (Nabertherm GmbH). A 20 % oxidation loss of Mg was assumed in accordance with the experiments in previous publications by other authors [6, 10, 46]. The concentration of some relevant impurities in the Al5N-Grade aluminum is given in Table 1. Phosphorous was added in the form of an Al-Cu-P master alloy with chemical composition given in Table 2. The nominal phosphorous contents of the eight test alloys were 0, 5, 20, 40, 60, 80, 100 and 500 ppm.

Table 1: Concentration of some relevant impurities in Al5N-Grade aluminium measured by glow discharge mass spectrometry (GDMS).

Ca	Cu	Mn	Fe	P
< 20 ppb	2.6 ppm	47 ppb	504 ppb	526 ppb

Table 2: Chemical composition of the Al-Cu-P master alloy measured by optical emission spectrometry (OES) at Hydro Aluminium Sunndalsøra.

Al	Cu	P
79.6 wt%	19.0 wt%	1.4 wt%

Aluminium was melted at 750 °C. Subsequently, SoG Si was added and the melt was thoroughly stirred with a graphite rod. The melt was stirred every few minutes until complete dissolution of the Si was achieved. Cubes of high purity Mg wrapped in aluminium foil were added to the melt and held below the surface in order to minimize oxidation. After the Mg addition, the melt was stirred thoroughly with a graphite rod. After holding at 750 °C for 10 minutes the Al-Cu-P master alloy was added and the melt was stirred for 30 seconds with a graphite rod. After 15 minutes the melt was skimmed and thermal analysis was performed.

3.2 Thermal analysis

Thermal analysis was performed in boron nitride coated stainless steel crucibles with bottom diameter 24 mm, top diameter 34 mm and height 33 mm. They were preheated at 700 °C in a Nabertherm K1 resistance furnace, and placed on top of the melt in order to reach thermal equilibrium with the alloy. The stainless steel crucibles were filled with the molten alloy and placed on an insulating Fiberfrax board (Unifrax I LLC). A boron nitride coated type K thermocouple was lowered centrally into the melt and fixed with the tip 10 mm from the bottom of the crucible. Another Fiberfrax board was placed on top of the crucible as shown in Figure 12.

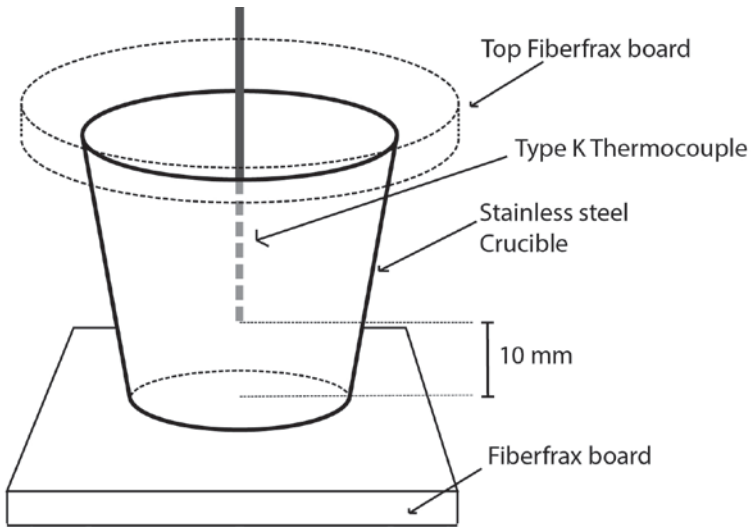

Figure 12: Sketch of the experimental setup during thermal analysis. A boron nitride coated stainless steel crucible was placed between two Fiberfrax boards and the temperature was measured by a Type K thermocouple.

The temperature data was recorded with a frequency of 50 Hz with a Campbell CR23X datalogger (Campbell Scientific, Inc.). The data was transferred to a computer through the Campbell Scientific PC400 4.1 Software.

The thermocouple was calibrated in high purity aluminium (assuming a melting point of 660.0 °C) before and after each set of experiments to record eventual temperature drift, and the calibration results were applied to the recorded temperatures during thermal analysis. The cooling curves were analyzed by the use of the Thermal Analysis for Windows (TAW32) software developed by Alutron. The data was averaged with the software yielding a logging frequency of 10 Hz and the first derivative (dT/dt) was calculated.

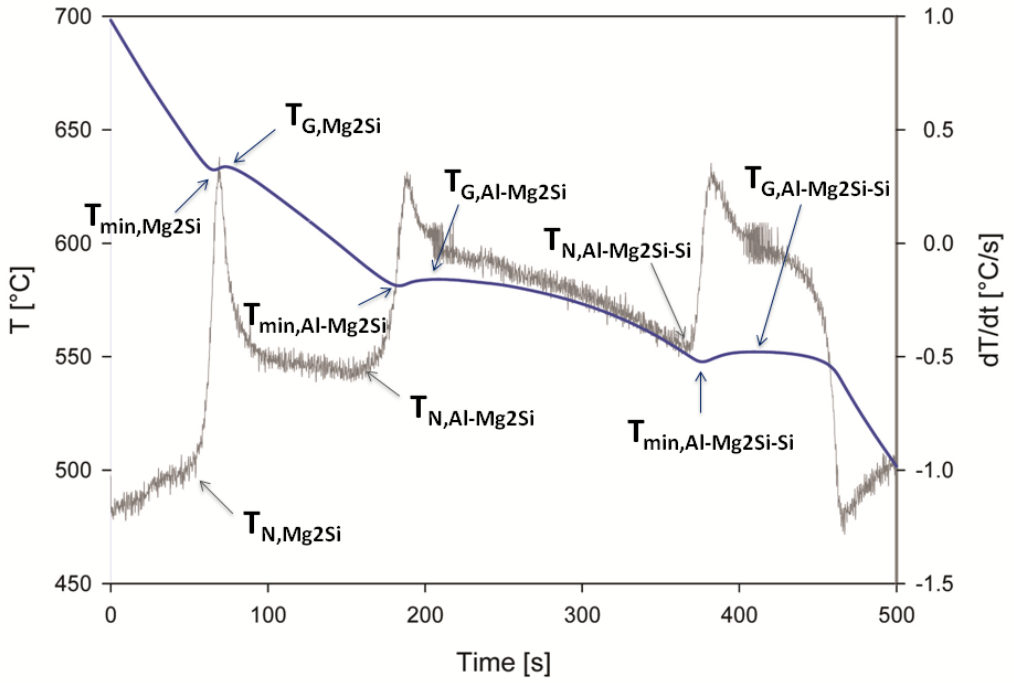

Figure 13: Typical solidification curve with associated first derivative for a Al-15Mg_2Si-5Si alloy. The nucleation temperature is found as the temperature where the first derivative (dT/dt) starts to increase rapidly, indicating release of latent heat.

Figure 13 shows a typical solidification curve for Al-15Mg_2Si-5Si with the characteristic temperatures as defined in Table 3. The three main reactions are the precipitation of primary Mg_2Si, the binary Al-Mg_2Si eutectic reaction and the ternary Al-Mg_2Si-Si reaction.

Table 3: Definition of the characteristic temperatures from the thermal analysis.

Symbol	Description
$T_{N,Mg2Si}$	Nucleation temperature for primary Mg_2Si
$T_{min,Mg2Si}$	Minimum temperature of the primary Mg_2Si phase
$T_{G,Mg2Si}$	Growth temperature primary Mg_2Si
$\Delta T_{R,Mg2Si}$	Recalescence undercooling of the primary Mg_2Si phase (= $T_{G,Mg2Si}$ - $T_{min,Mg2Si}$)
$T_{N,Al-Mg2Si}$	Nucleation temperature for the binary Al – Mg_2Si eutectic
$T_{min,Al-Mg2Si}$	Minimum temperature of the binary Al – Mg_2Si eutectic
$T_{G,Al-Mg2Si}$	Growth temperature for the binary Al – Mg_2Si eutectic
$\Delta T_{R,Al-Mg2Si}$	Recalescence undercooling of the binary eutectic (= $T_{G,Al-Mg2Si}$ - $T_{min,Al-Mg2Si}$)
$T_{N,Al-Mg2Si-Si}$	Nucleation temperature for the ternary Al - Mg_2Si – Si eutectic
$T_{min,Al-Mg2Si-Si}$	Minimum temperature of the ternary Al - Mg_2Si – Si eutectic
$T_{G,Al-Mg2Si-Si}$	Growth temperature for the ternary Al - Mg_2Si – Si eutectic
$\Delta T_{R,Al-Mg2Si-Si}$	Recalescence undercooling of the ternary eutectic (= $T_{G,Al-Mg2Si-Si}$ - $T_{min,Al-Mg2Si-Si}$)

3.3 Microstructural analysis

The cast microstructural samples were sectioned along the center vertical plane using a Struers Discotom-5 (Struers A/S) with a 10S25 cutting disk. The specimens were plane ground on a Struers Rotopol-31 with P80, P120, P320, P500 and P1200 SiC grinding paper. They were further polished with a Struers Tegrapol-31. The polishing was performed according to the sequence given in Table 4 and the samples were cleaned thoroughly in an ultrasonic bath filled with ethanol between each step. The OP-S Diapro used is a colloidal silica suspension (0.04 µm particle size) with pH 9.8. After OP-S the specimens were immediately cleaned with ethanol in order to avoid excessive etching.

Table 4: Preparation steps for polishing with Struers Tegrapol-31.

Polishing disk	Diapro	Time
MD Largo	6 µm	6 min
MD Mol	3 µm	10 min
MD Chem	OP-S	1 min

Microstructural characterization was done in a Leica MEF4M inverted light microscope (Leica Microsystems GmbH), and pictures were taken with a Jenoptik ProgRes C10 plus camera (Jenoptik Optical Systems GmbH). The positioning within the specimen was measured with a Sony LH51-2 display unit (Sony Precision Technology Inc.), measuring the displacement of the Leica MEF4M specimen table.

Microstructural specimens were deep-etched in a 20 % NaOH aqueous solution for 120 minutes to remove the aluminium matrix. The specimens were cleaned in an ultrasonic bath filled with ethanol for 10 minutes to break up the loose eutectic structures and remove particles from the surface. The deep-etched specimens were examined by secondary electron imaging in a Zeiss Supra 55 VP LVFESEM (Carl Zeiss AG).

3.4 Chemical analysis

Wavelength Dispersive Spectroscopy (WDS)

The specimens were coated with carbon and examined in a JEOL JXA-8500F Electron Probe Micro Analyzer (EPMA) equipped with 5 WDS detectors (JEOL Ltd.).

Element maps of approximate area 800 x 800 μm^2 of the elements Al, Mg, Si, P and Mn were recorded. Element maps of approximate area 400 x 400 μm^2 of the elements Al, Mg, P, Mn, Si, Cu, Fe and O were also recorded. A probe current of $3.0 \cdot 10^{-8}$ A with 15 kV accelerating voltage was used. The specimens were examined in backscatter electron

imaging (BEI) mode to find particles rich in phosphorous. Element maps of approximate area 80 x 80 μm^2 of the elements Al, Mg, Si, P and O were recorded centered on the identified particles. To avoid destroying the P rich particles 10 kV accelerating voltage was used for the detailed element maps.

Glow Discharge Mass Spectrometry (GDMS)

The chemical composition of the alloys was analyzed by a Finnigan ELEMENT GD (Thermo Fisher Scientific Inc.). Prior to analysis, the samples were plane ground with P500 SiC grinding paper and thoroughly cleaned in an ultrasonic bath filled with ethanol.

During a GDMS analysis the surface of the sample is sputtered by argon ions. The atoms from the sample are ionized in the plasma, extracted and channeled towards the mass analyzer. The mass analyzer consists of a set of detectors counting the ions based on their mass. The argon discharge gas flow was 395 ml/min, the discharge current 67.3 mA and the discharge voltage varied between 525 and 551 V. The isotopes analyzed were ^{24}Mg, ^{28}Si, ^{31}P, ^{44}Ca, ^{56}Fe and ^{63}Cu.

The quantification of the impurity concentration was calculated from the intensities (counts per second) of aluminium (I_{Al}) and the impurity element (I_X), the abundances of aluminium (A_{Al}) and the impurity element (A_X) and the relative sensitivity factor of the impurity element (RSF_X) according to Equation 5. The RSFs were found by analyzing five different standard samples with tabulated phosphorous concentrations between 10 and 56 ppm, and calculated according to the procedure found in Ref. [47]. The tabulated concentrations of all the analyzed isotopes in the standard alloys are provided in Appendix 1.

$$c_X\,(ppm) = 10^6 \cdot \frac{I_X}{I_{Al}} \cdot \frac{A_{Al}}{A_X} \cdot RSF_X \qquad \textit{(Eq. 5.)}$$

The sputtering rate for the parameters used in these analyses was approximately 1 μm/min. A presputtering time of 2 minutes was used to remove eventual oxide layers and obtain a stable signal. The total analysis time was 24 minutes, resulting in a sputtering depth of approximately 22 μm. The sputtered area on the sample surface is circular with diameter 7 mm.

Optical Emission Spectrometry (OES)

The Mg and Si content in the test alloys was analyzed by OES at Hydro Aluminium Sunndalsøra for better accuracy at high concentrations. No standard program for analysis of alloys with both high Mg and high Si content was available. The *ALALMG* program, which is calibrated for high Mg contents (up to approximately 18 wt%) and moderate Si contents (up to approximately 2 wt%) was the most suitable program for the Al-15Mg_2Si-5Si alloys and was therefore used for quantification.

4 Results

4.1 Microstructural characterization

4.1.1 Macrostructure of the Al-15Mg_2Si-5Si castings

Figure 14 shows the macrostructure of the cast alloys. There is an evident macrosegregation of primary Mg_2Si particles to the top of the specimen. In the images for the alloys with 40 and 80 ppm P, the position of the thermocouple is seen. It is clear that the primary Mg_2Si particles agglomerate closer to the top of the specimen with increasing phosphorous content. As the melt was not degassed before casting, the alloys contain a relatively large amount of gas porosity visible by the black areas in the interior of the specimens.

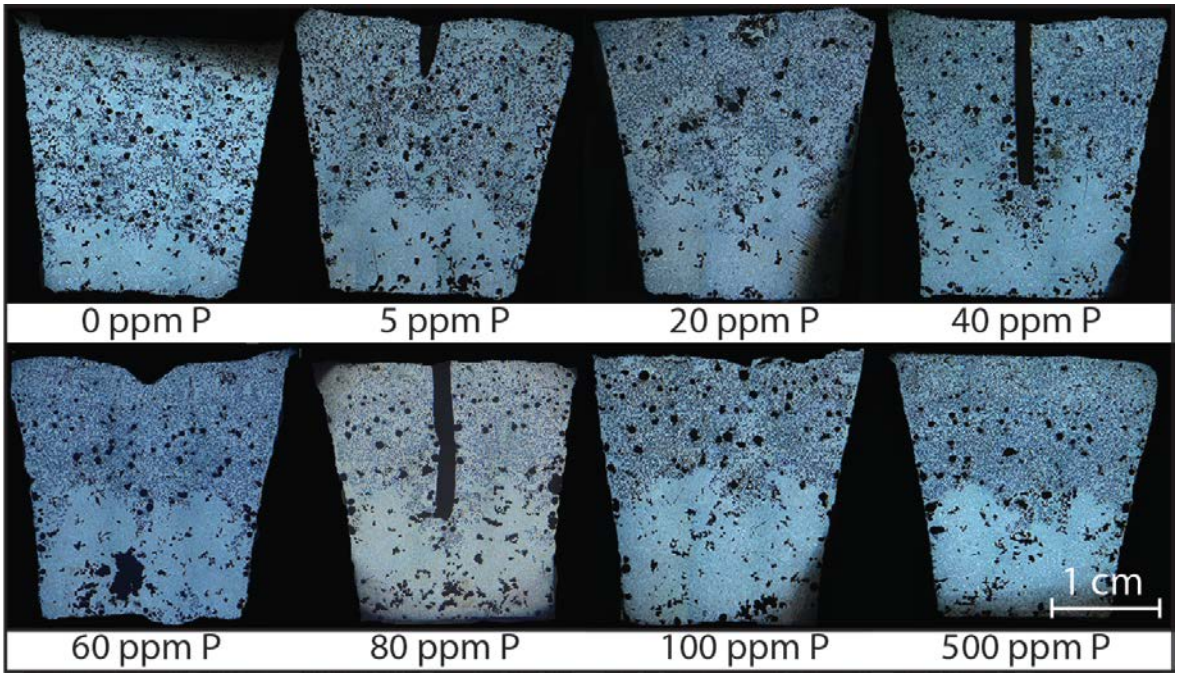

Figure 14: Macrostructures of the cast alloys. There is a clearly visible macrosegregation of the primary Mg_2Si particles to the top of the specimens. The black areas in the interior of the specimens are pores.

The metallographic specimens showed a large tendency for macrosegregation with no primary Mg_2Si particles located in the lower 5 – 10 mm of the cast specimens. In specimens with both dendritic and polygonal primary Mg_2Si, the polygonal particles were located higher in the specimen relative to the dendritic primary Mg_2Si. This was observed in the alloys with 5, 20, 40, 60, 80 and 100 ppm P. The alloy with 5 ppm P had only a few polygonal particles located at the very top of the cast specimen. The fraction of the primary Mg_2Si particles with a polygonal morphology is shown in Figure 15. In the

alloy without phosphorous addition the Mg_2Si particles exhibit a purely dendritic morphology, whilst in the alloy with 500 ppm added phosphorous all the particles have a polygonal morphology.

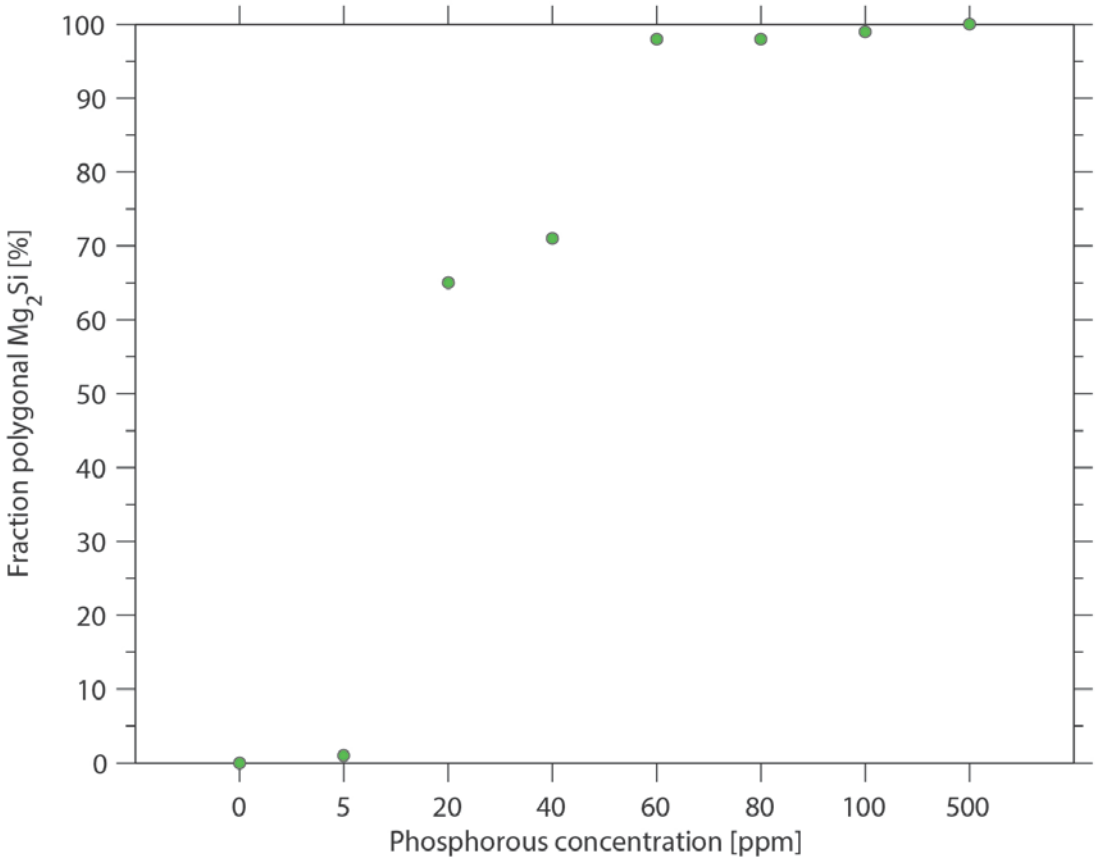

Figure 15: Fraction of the primary Mg_2Si particles with polygonal morphology in the test alloys. The base Al-15Mg_2Si-5Si alloy without P addition showed a purely dendritic morphology, whilst all the primary Mg_2Si particles were polygonal with the addition of 500 ppm P.

The number of Mg_2Si particles was counted over a representative image of a real area of 13.83 mm^2, and the calculated number densities are shown in Table 5. The area fraction of the macroscopic images where primary Mg_2Si particles are located was used to calculate an average number density for the whole specimen cross section. This is necessary as the number density varies greatly over the cross section due to macrosegregation. The fraction of polygonal Mg_2Si particles was found from image analysis of the macroscopic images by the ImageJ 1.47v software.

Table 5: Calculated number density of primary Mg_2Si and fraction of the primary Mg_2Si with polygonal morphology in the specimens. (* The number density of dendritic Mg_2Si is only approximate as interpreting which areas that belong to which dendrite is difficult in optical microscopy)

P addition	Number density, Primary Mg_2Si	$f_{polygonal\ Mg_2Si}$
0 ppm	1-2 particles · mm^{-2} *	0 %
5 ppm	2-4 particles · mm^{-2} *	1 %
20 ppm	36 particles · mm^{-2}	65 %
40 ppm	41 particles · mm^{-2}	71 %
60 ppm	46 particles · mm^{-2}	98 %
80 ppm	43 particles · mm^{-2}	98 %
100 ppm	43 particles · mm^{-2}	99 %
500 ppm	46 particles · mm^{-2}	100 %

4.1.2 Primary Mg_2Si particles

The microstructures found next to the thermocouple tip in the specimens are shown in Figure 16 - Figure 23. The microstructure in the specimen without added phosphorous consist of coarse dendritic primary Mg_2Si particles, a binary eutectic and a ternary eutectic. A slight refinement of primary Mg_2Si is observed with addition of 5 ppm P. The dendrites are smaller in the primary directions, compared with the specimen without added P. Figure 18 and Figure 19 show a further refinement with 20 and 40 ppm P added, respectively. In the specimen with 60 ppm P, 98 % of the primary Mg_2Si particles are polygonal. Figure 21 - Figure 23 show the further refinement of the polygonal Mg_2Si particles with increasing phosphorous content. In the specimen with 500 ppm P added, all the primary Mg_2Si particles are polygonal. The black areas in the microstructural images are pores in the material present as the melt was not degassed before casting.

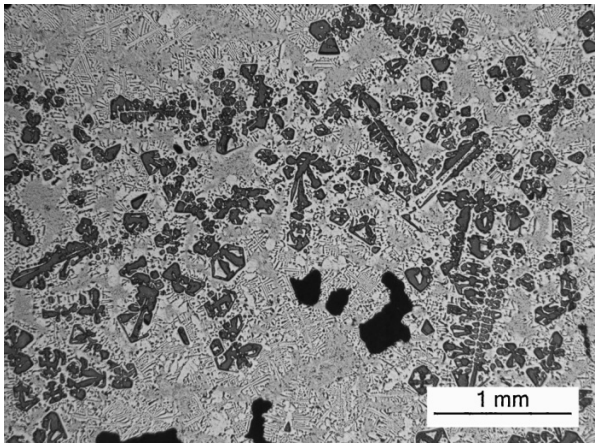

Figure 16: Microstructure of Al-15Mg_2Si-5Si without phosphorous addition. Coarse primary Mg_2Si dendrites.

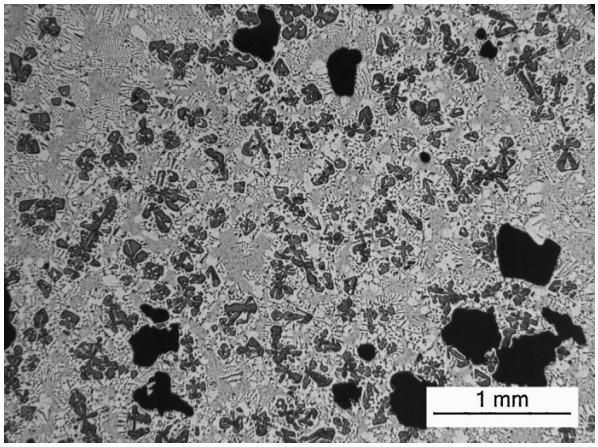

Figure 17: Microstructure of Al-15Mg_2Si-5Si with addition of 5 ppm phosphorous. Slight refinement of primary Mg_2Si, and more fractioned dendrites.

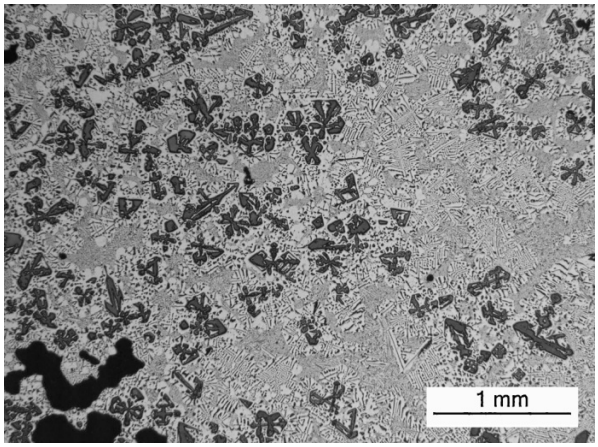

Figure 18: Microstructure of Al-15Mg_2Si-5Si with addition of 20 ppm phosphorous. Refined and partly modified primary Mg_2Si particles.

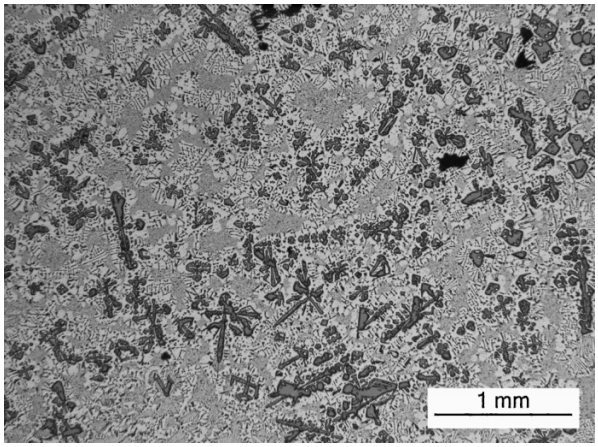

Figure 19: Microstructure of Al-15Mg_2Si-5Si with addition of 40 ppm phosphorous. Refined and partly modified primary Mg_2Si particles.

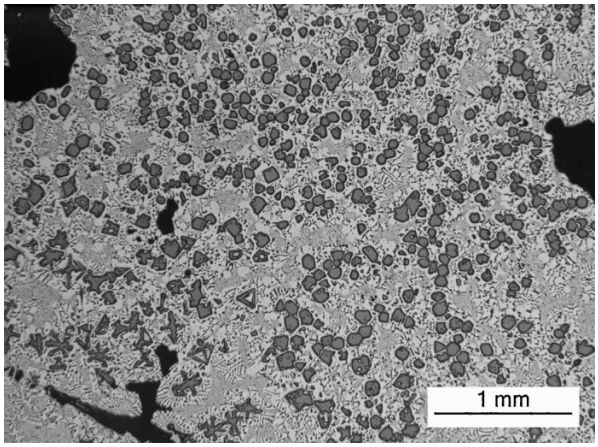

Figure 20: Microstructure of Al-15Mg_2Si-5Si with addition of 60 ppm phosphorous. Considerably refined primary Mg_2Si with a large fraction of polygonal particles.

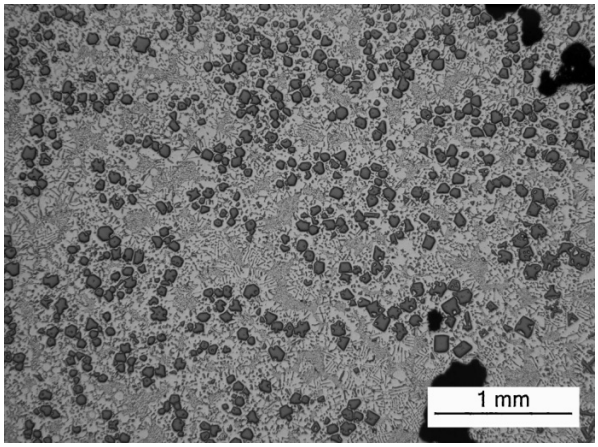

Figure 21: Microstructure of Al-15Mg_2Si-5Si with addition of 80 ppm phosphorous. Refined primary Mg_2Si relative to the specimen with 80 ppm P. Mainly polygonal primary Mg_2Si particles.

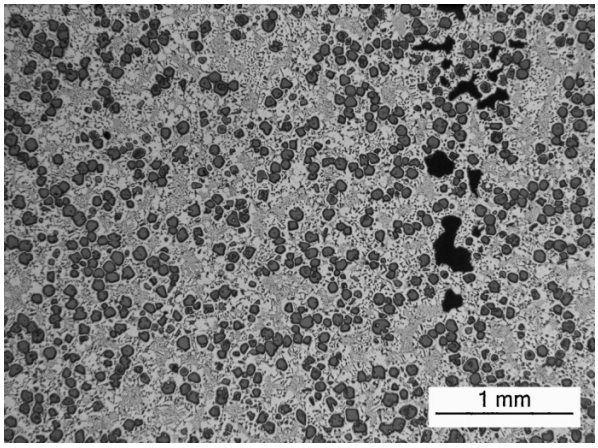

Figure 22: Microstructure of Al-15Mg_2Si-5Si with addition of 100 ppm phosphorous. Mainly polygonal primary Mg_2Si particles.

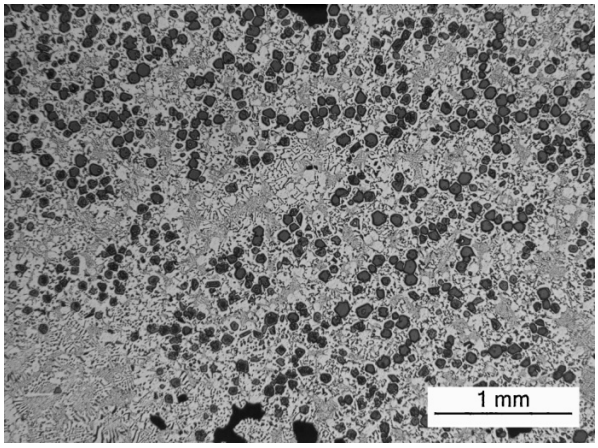

Figure 23: Microstructure of Al-15Mg_2Si-5Si with addition of 500 ppm phosphorous. Smaller polygonal primary Mg_2Si particles relative to the specimen with 100 ppm P.

Figure 24 - Figure 31 show larger magnification optical micrographs of the primary Mg_2Si particles. Figure 24 clearly shows the faceted dendritic morphology of the primary Mg_2Si particles. The secondary dendrite arm spacing (SDAS) is used as a measure for particle size of the dendritic particles. The average SDAS was measured as the average arm spacing along the longest primary direction in the micrographs. The average SDAS in the specimen without added phosphorous is 112 µm. In Figure 25 and Figure 26, the dendrites are smaller in the primary directions relative to the alloy without added phosphorous. As the dendrites are more equiaxed, no reliable measurements for the average SDAS were possible. Figure 27 - Figure 31 show that the polygonal Mg_2Si particles gradually decrease in average size, from 49 µm with 40 ppm P to 43 µm with 500 ppm P.

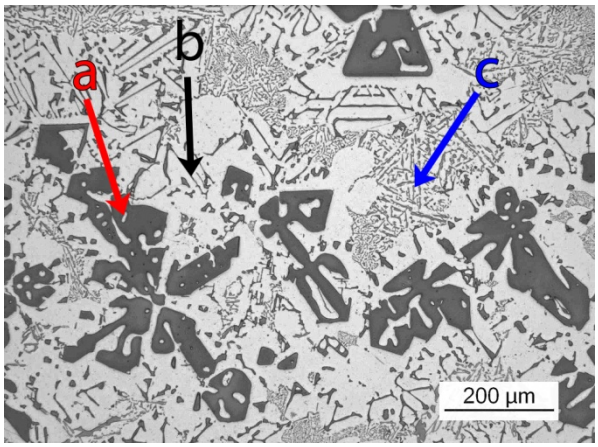

Figure 24: Microstructure of Al-15Mg_2Si-5Si without phosphorous addition. Coarse faceted primary Mg_2Si dendrites (a), the binary Al-Mg_2Si eutectic (b) and the ternary Al-Mg_2Si-Si eutectic (c) are indicated by the arrows.

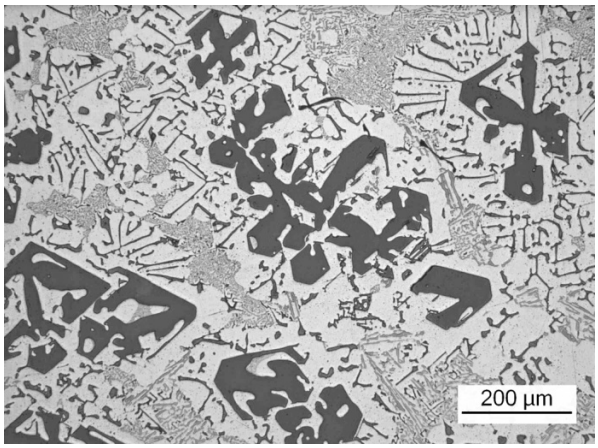

Figure 25: Microstructure of Al-15Mg_2Si-5Si with addition of 5 ppm phosphorous. Slight refinement of primary Mg_2Si relative to the specimen with no phosphorous addition.

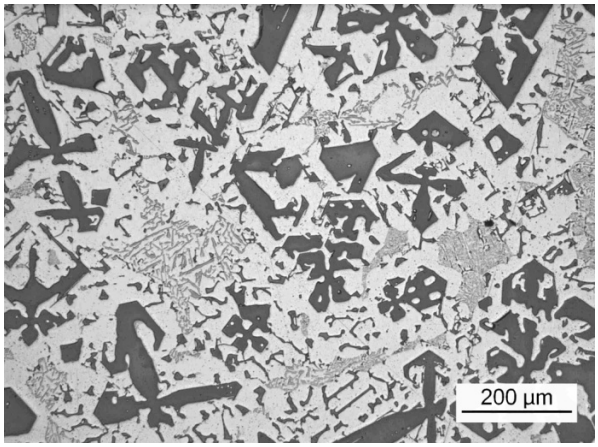

Figure 26: Microstructure of Al-15Mg_2Si-5Si with addition of 20 ppm phosphorous. Refined and partly modified primary Mg_2Si particles with fractioned dendrites.

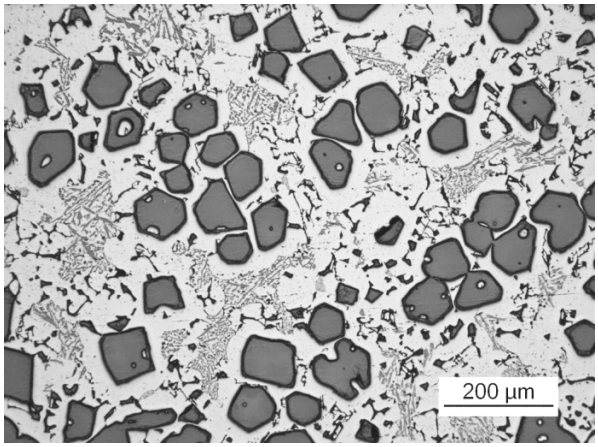

Figure 27: Microstructure of Al-15Mg_2Si-5Si with addition of 40 ppm phosphorous. Polygonal primary Mg_2Si particles of average size 49 µm.

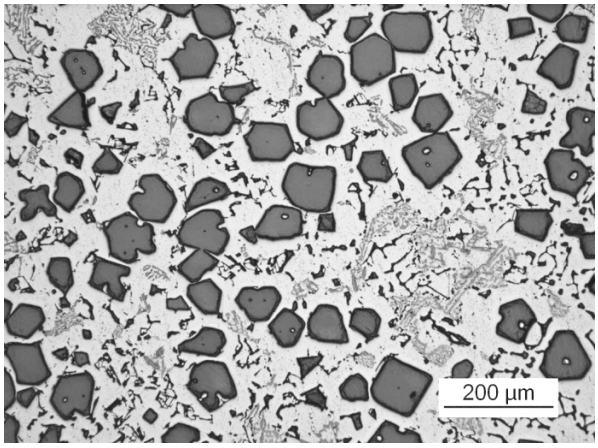

Figure 28: Microstructure of Al-15Mg_2Si-5Si with addition of 60 ppm phosphorous. Polygonal primary Mg_2Si particles of average size 48 µm.

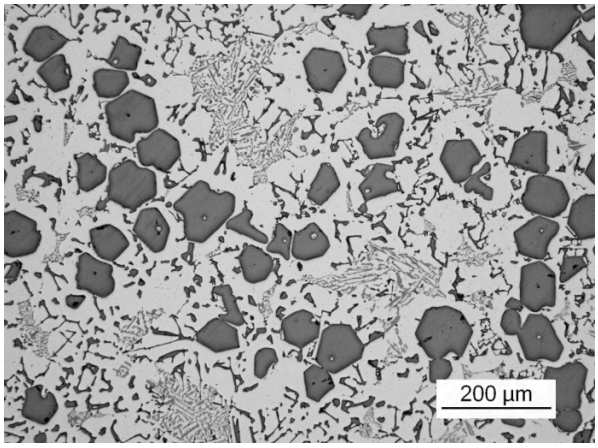

Figure 29: Microstructure of Al-15Mg_2Si-5Si with addition of 80 ppm phosphorous. Polygonal primary Mg_2Si particles of average size 48 µm.

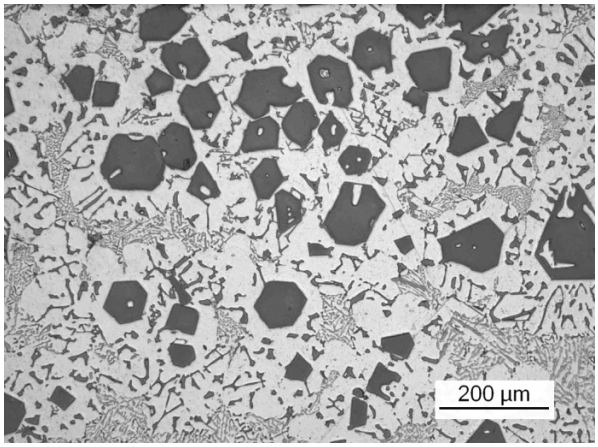

Figure 30: Microstructure of Al-15Mg_2Si-5Si with addition of 100 ppm phosphorous. Polygonal primary Mg_2Si particles of average size 47 µm.

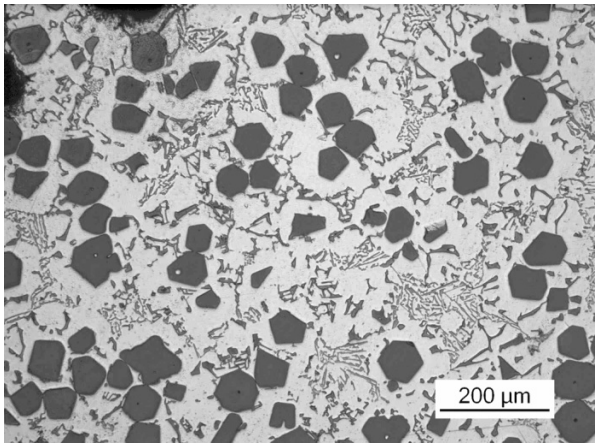

Figure 31: Microstructure of Al-15Mg_2Si-5Si with addition of 500 ppm phosphorous. Considerably refined polygonal primary Mg_2Si particles relative to the 100 ppm P specimen. The average particle size is 43 µm.

4.1.3 The eutectic structures

Figure 32 - Figure 39 show the binary and ternary eutectic structures approximately 5 mm below the thermocouple tip. The binary Al-Mg_2Si eutectic is mainly a lamellar irregular eutectic with the dark phase being Mg_2Si and the white phase being Al. The Mg_2Si lamellae grew with a faceted morphology. In the specimen without phosphorous addition a large fraction of the binary Al-Mg_2Si eutectic has a fibrous morphology (indicated by the arrow in Figure 32). These fibrous structures are less prevalent in the other alloys as seen in Figure 33 - Figure 39. The ternary Al-Mg_2Si-Si eutectic is irregular and consists mainly of faceted Si lamellae and Al. Apart from the fibrous binary eutectic in the specimen without phosphorous, no clear differences in the eutectic structures were observed between the samples.

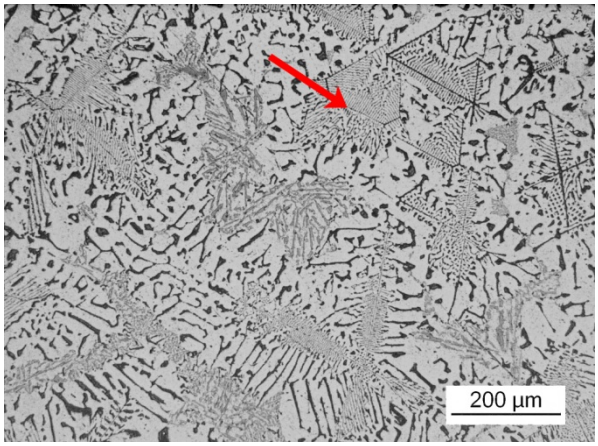

Figure 32: Eutectic microstructure of Al-15Mg_2Si-5Si without phosphorous addition. A large fraction of the binary Al-Mg_2Si eutectic has a fibrous morphology indicated by the arrow.

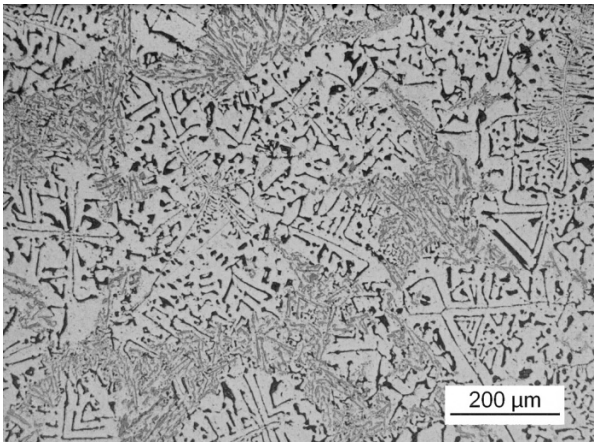

Figure 33: Eutectic microstructure of Al-15Mg_2Si-5Si with addition of 5 ppm phosphorous. Irregular binary and ternary eutectic.

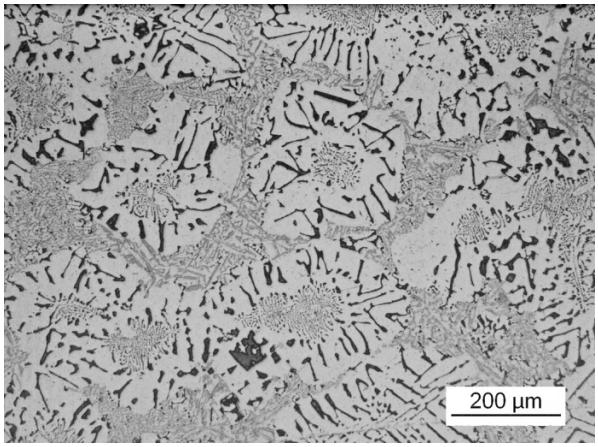

Figure 34: Eutectic microstructure of Al-15Mg_2Si-5Si with addition of 20 ppm phosphorous. Irregular binary and ternary eutectic.

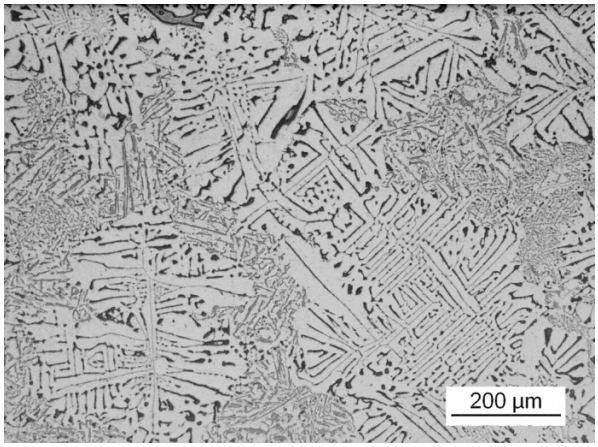

Figure 35: Eutectic microstructure of Al-15Mg_2Si-5Si with addition of 40 ppm phosphorous. Irregular binary and ternary eutectic.

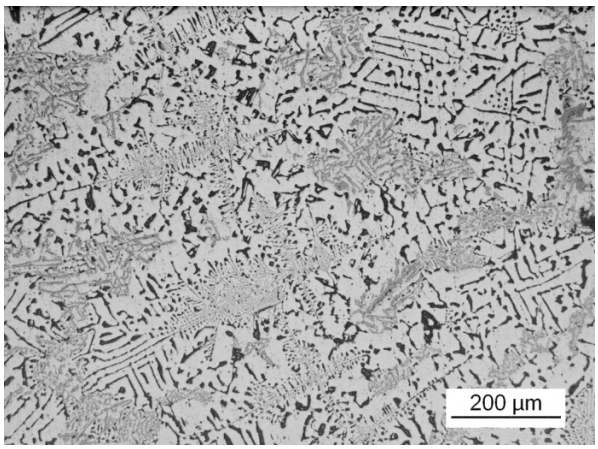

Figure 36: Eutectic microstructure of Al-15Mg_2Si-5Si with addition of 60 ppm phosphorous. Irregular binary and ternary eutectic.

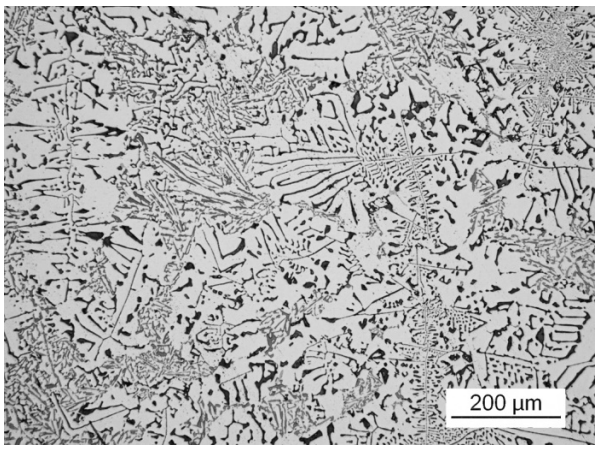

Figure 37: Eutectic microstructure of Al-15Mg_2Si-5Si with addition of 80 ppm phosphorous. Irregular binary and ternary eutectic.

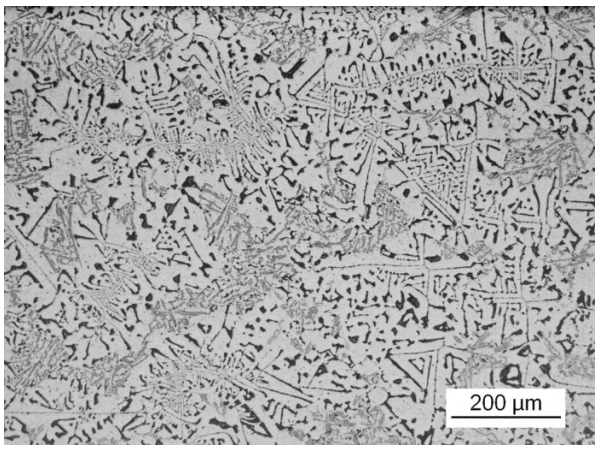

Figure 38: Eutectic microstructure of Al-15Mg_2Si-5Si with addition of 100 ppm phosphorous. Irregular binary and ternary eutectic.

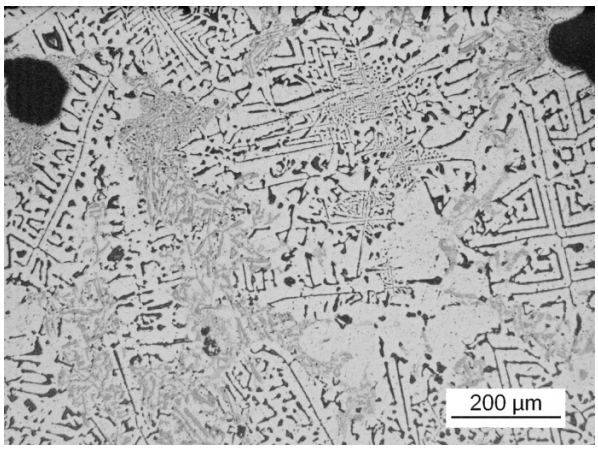

Figure 39: Eutectic microstructure of Al-15Mg_2Si-5Si with addition of 500 ppm phosphorous. Irregular binary and ternary eutectic.

4.1.4 Morphological characterization by deep-etching in 20 % NaOH

The various observed morphologies of the primary Mg_2Si particles are shown in the secondary electron images in Figure 40 - Figure 45. The morphologies of the Mg_2Si particles are characterized by faceted growth. The alloys with 0 and 5 ppm added phosphorous exhibit mainly dendritic morphologies. It can be observed that growth initially has occurred along the primary <100> directions, followed by growth in the <110> directions. The <110> directions lie in the {111} planes, meaning that the {111} planes develop between the initial <100> directions. This is illustrated by the arrows drawn in Figure 42. Different polygonal morphologies are observed, with the slightly truncated octahedron shown in Figure 44 and the tetrakaidecahedron shown in Figure 45 as two examples. With increasing phosphorous content, the tendency for polygonal primary Mg_2Si morphologies increases. Although all the specimens contain a mixture of different primary Mg_2Si morphologies, the tetrakaidecahedron was only observed in the alloy with 500 ppm added phosphorous.

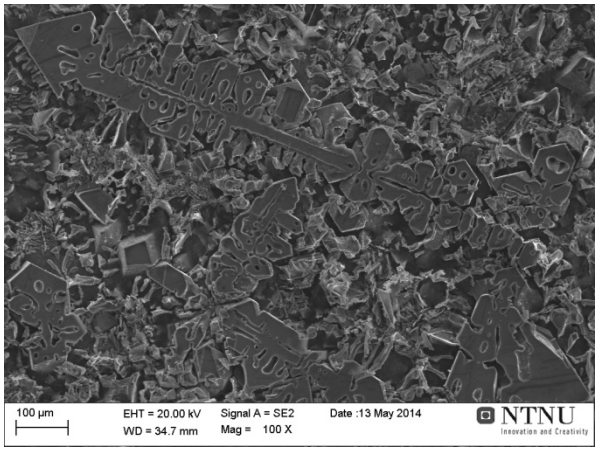

Figure 40: Secondary electron image of large dendrites observed in the alloy without added phosphorous.

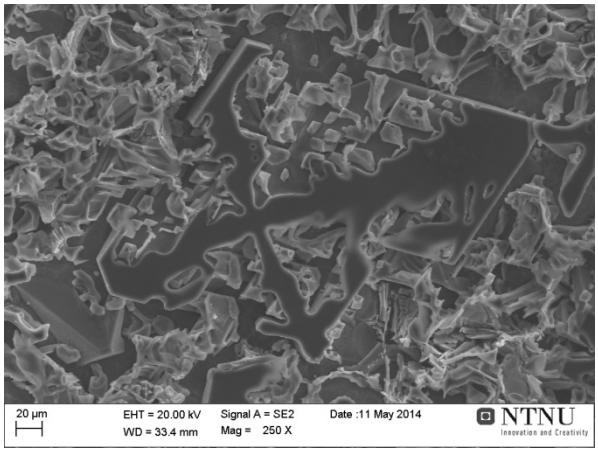

Figure 41: Higher magnification image of a dendritic primary Mg_2Si particle in the alloy with 5 ppm P. The faceted morphology is evident.

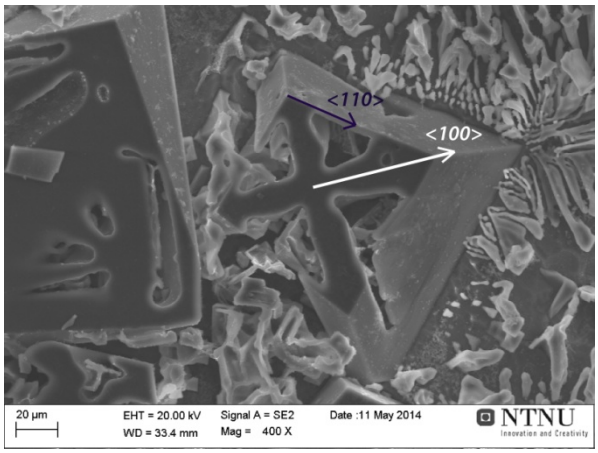

Figure 42: Equiaxed dendritic morphology in the alloy with 5 ppm added phosphorous. After initial growth along the <100> directions the {111} faces develop, bounding the Mg_2Si particle, leaving holes in the crystal between the centre and the outer {111} faces.

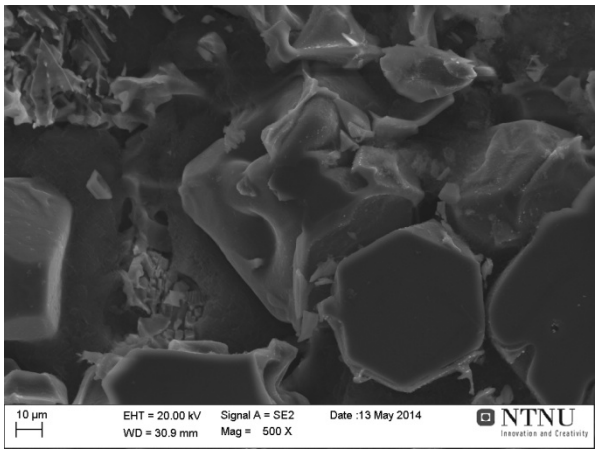

Figure 43: Equiaxed dendritic morphology in the alloy with 80 ppm added phosphorous. As in Figure 42 growth proceeds slowly in the center of the {111} faces producing a hopper-like particle.

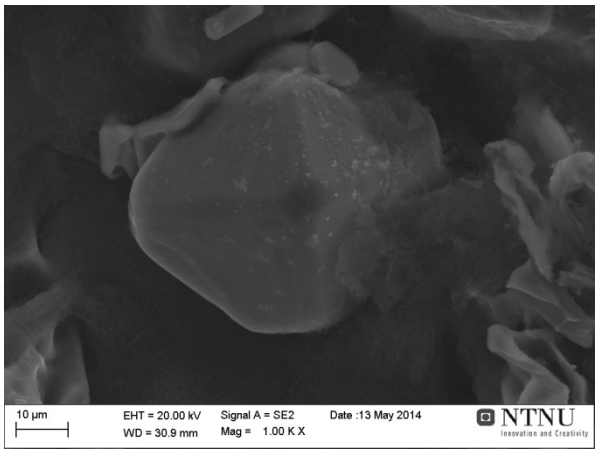

Figure 44: Octahedral primary Mg_2Si particle observed in the alloy with 80 ppm added phosphorous. The corners are slightly truncated.

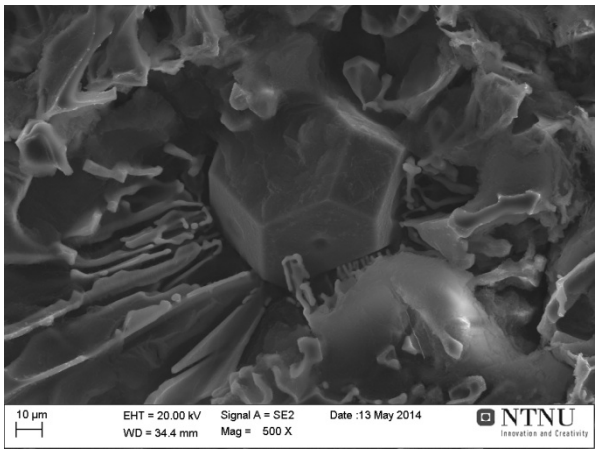

Figure 45: Polygonal primary Mg_2Si particle observed in the alloy with 500 ppm added phosphorous. The particle morphology is identified as a tetrakaidecahedron.

4.2 Thermal analysis

Thermal analysis showed three main reactions during solidification: Precipitation of primary Mg_2Si, the binary Mg_2Si - Al eutectic reaction and the ternary Mg_2Si - Al - Si eutectic reaction. Four subsequent thermal analyses were performed on each alloy and all cooling curves are reproducible within ± 0.4 °C. The cooling rate prior to solidification was 1.3 K/s in all the experiments. The recorded curves for the first thermal analysis for each alloy are presented in Figure 46 - Figure 53.

For the alloys with 5, 20 and 40 ppm added phosphorous, an additional reaction was observed in the primary crystallization field of Mg_2Si. These secondary reaction peaks are highlighted by the circles in Figure 47 - Figure 49. The temperature interval of this reaction decreased with increasing phosphorous content from 635 °C - 620 °C for 5 ppm, to 612 °C - 595 °C for 20 ppm and 605 °C - 584 °C for 40 ppm.

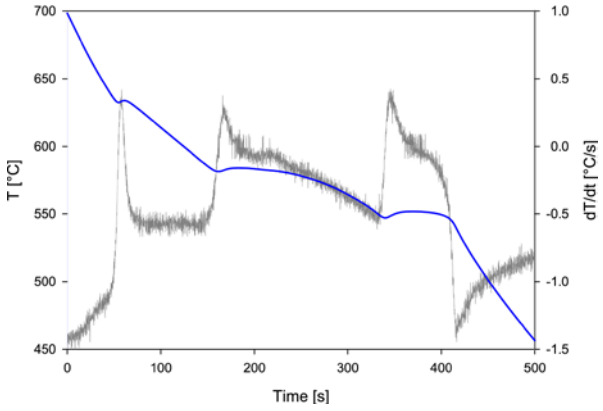

Figure 46: Solidification curve and associated first derivative for the alloy with no phosphorous added.

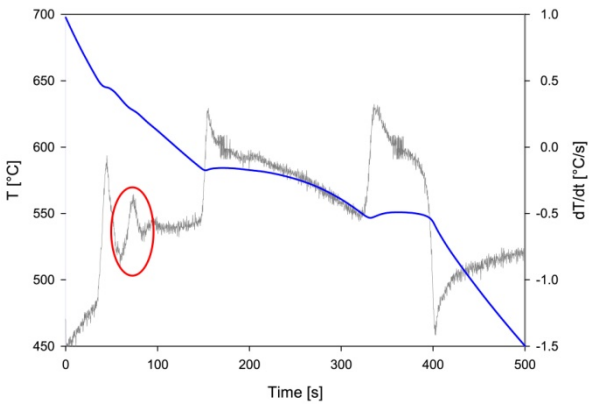

Figure 47: Solidification curve and associated first derivative for the alloy with 5 ppm phosphorous added. The secondary reaction peak is highlighted.

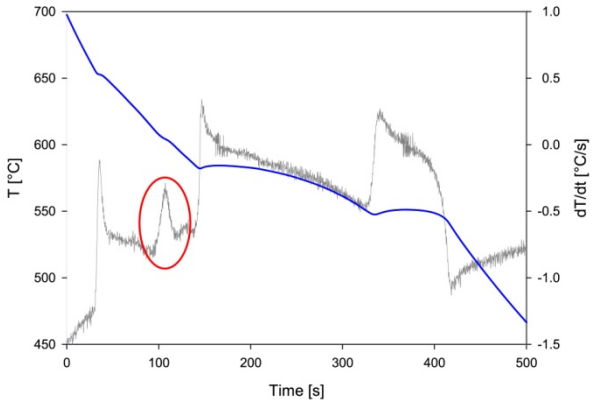

Figure 48: Solidification curve and associated first derivative for the alloy with 20 ppm phosphorous added. The secondary reaction peak is highlighted.

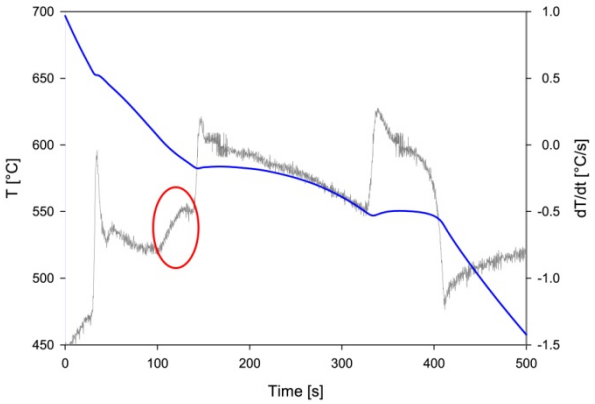

Figure 49: Solidification curve and associated first derivative for the alloy with 40 ppm phosphorous added. The secondary reaction peak is highlighted.

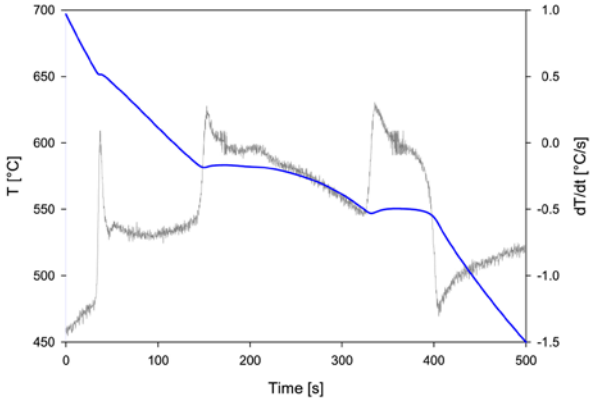

Figure 50: Solidification curve and associated first derivative for the alloy with 60 ppm phosphorous added.

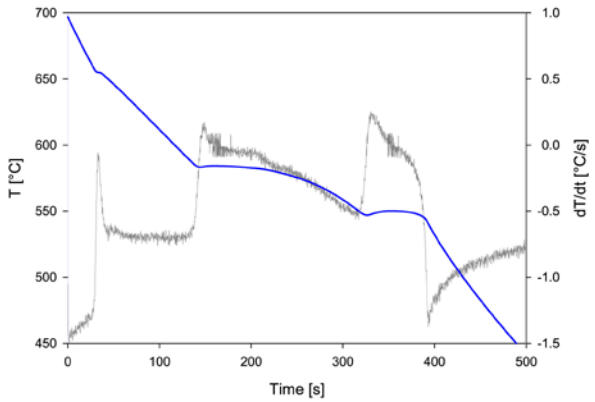

Figure 51: Solidification curve and associated first derivative for the alloy with 80 ppm phosphorous added.

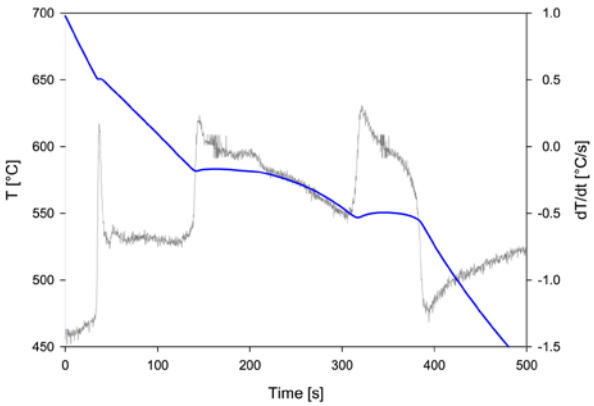

Figure 52: Solidification curve and associated first derivative for the alloy with 100 ppm phosphorous added.

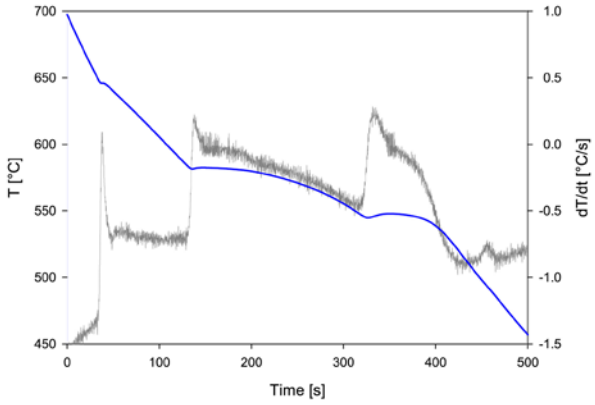

Figure 53: Solidification curve and associated first derivative for the alloy with 500 ppm phosphorous added.

The measured characteristic temperatures during thermal analysis are summarized in Figure 55 - Figure 57, with the values presented in Appendix 2. The nucleation temperature for primary Mg_2Si increases from 640.6 °C without P addition to 651.2 °C with 5 ppm P added. It further increases to 656.4 °C for 20 ppm P added, and then decreases down to 649.3 °C for 500 ppm P. Sections of the solidification curves showing the start of the primary Mg_2Si reaction for the alloys with 0, 5 and 20 ppm P are shown in Figure 54. The measurements for the 80 ppm P specimen deviate from the neighboring samples by around + 4 °C for the primary Mg_2Si reaction and + 2 °C for the binary Al-Mg_2Si eutectic reaction. The recalescence undercooling is highest for the alloy without added P for all the three main reactions. No measurable recalescence is observed for the primary Mg_2Si reaction in the samples containing added P.

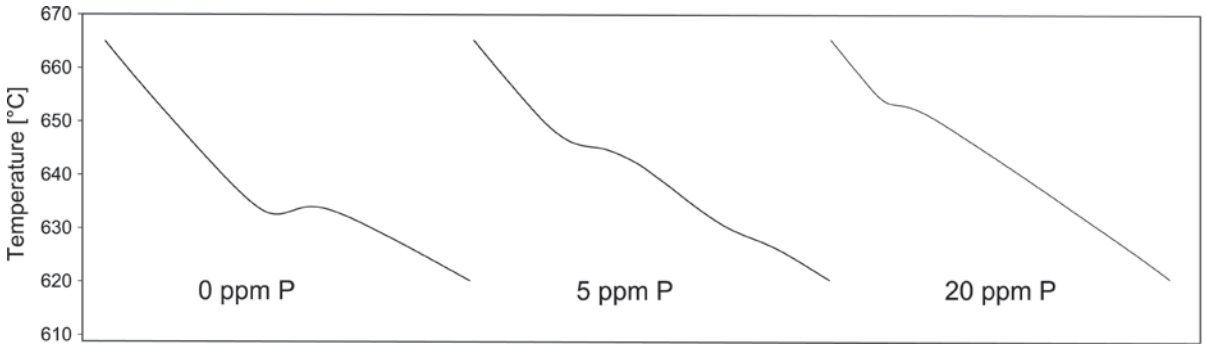

Figure 54: Part of the solidification curve associated with the primary Mg_2Si reaction for the alloys with 0, 5 and 20 ppm P. The time scale is normalized for clarification and each cooling curve section corresponds to approximately 65 seconds.

Figure 56 and Figure 57 show the characteristic temperatures for the binary and ternary eutectic reactions. The nucleation temperature for the Al-Mg_2Si binary eutectic reaction is lowered from 587.2 °C without added P to 584.6 °C with 5 ppm P added, and shows no further trend with increasing P content. The recalescence undercooling shows a tendency to decrease with increasing P content, from 2.8 K without P to 1.1 K with 500 ppm P added. The nucleation temperature for the Al-Mg_2Si-Si ternary eutectic reaction decreases gradually from 550.1 °C without added P to 547.2 °C with 500 ppm P added. The recalescence undercooling decreases from 4.2 K without added P to a minimum of 2.8 K with 500 ppm P added. The equilibrium temperature of the ternary eutectic reaction is 557 °C, which means that nucleation occurs at an undercooling of 6.9 K for the alloy without phosphorous.

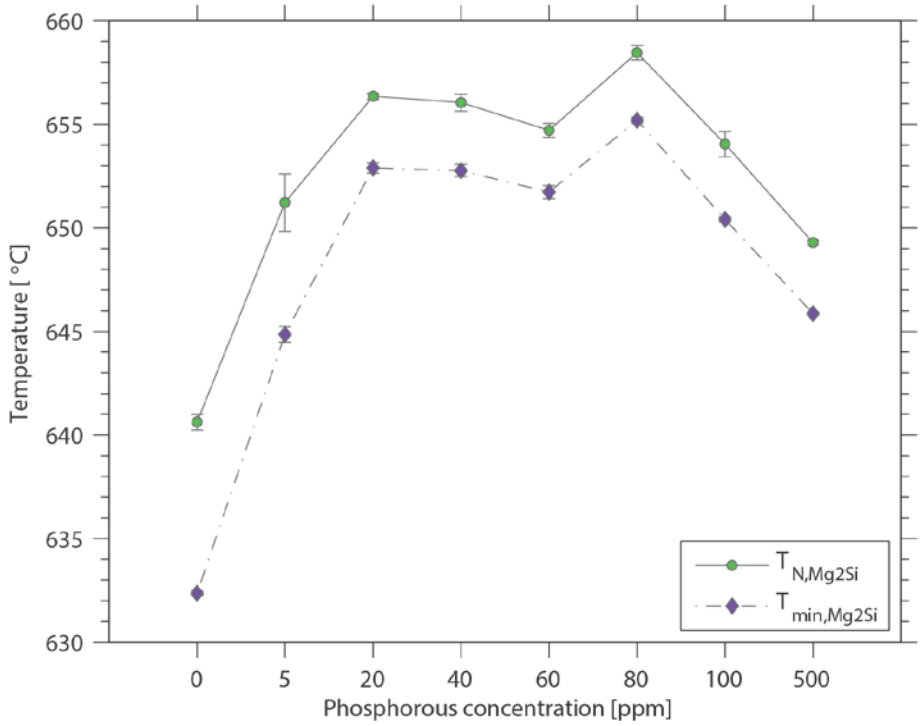

Figure 55: The nucleation and minimum temperatures for the primary Mg_2Si reaction in the alloys as a function of phosphorous content. A considerable increase in both the nucleation and minimum temperature up to 20 ppm P is observed.

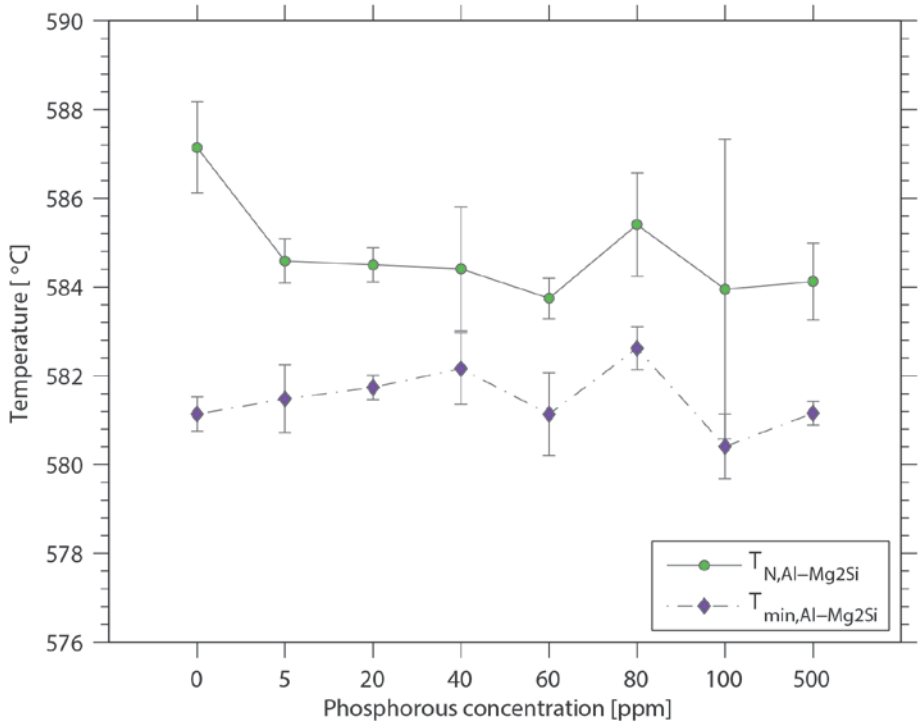

Figure 56: The nucleation and minimum temperatures for the binary Al-Mg_2Si eutectic reaction in the alloys as a function of phosphorous content. The nucleation temperature for the alloy without added phosphorous is higher than for the remaining alloys, which show no definite trend.

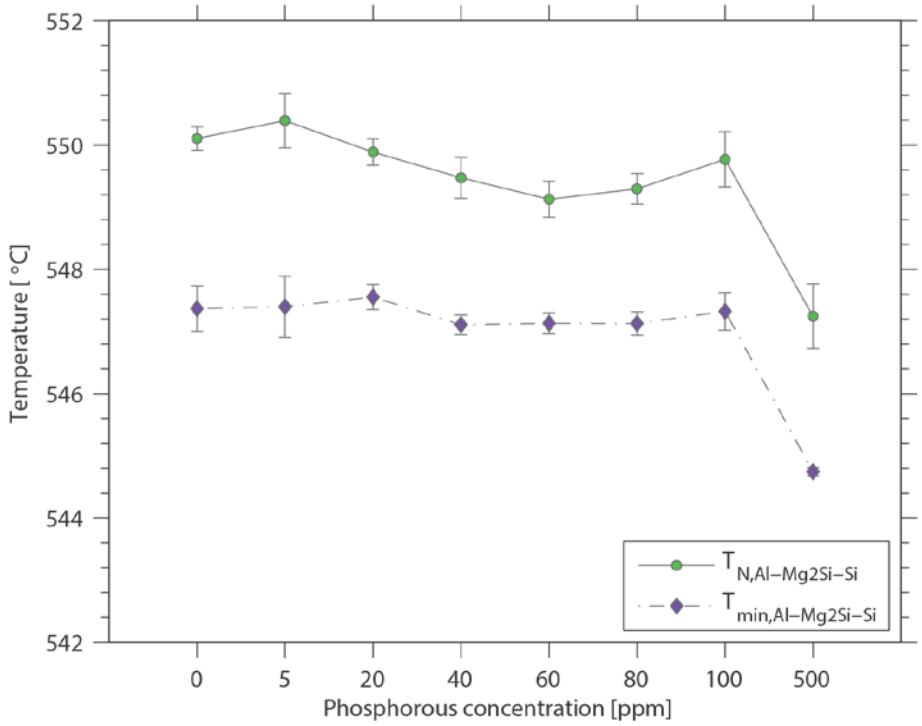

Figure 57: The nucleation and minimum temperatures for the ternary Al-Mg_2Si-Si eutectic reaction in the alloys as a function of phosphorous content. A slight decrease in the nucleation and minimum temperature with increasing P content is observed up to 100 ppm P. In the sample with 500 ppm P added both the nucleation and minimum temperatures are considerably reduced.

4.3 Chemical analysis

4.3.1 EPMA analysis

Figure 58 - Figure 61 show the element maps of Al, Mg, P, Mn and Si in the alloys with no added phosphorous, 5 ppm P, 100 ppm P and 500 ppm P added together with the backscattered electron images. The primary Mg_2Si dendrites are refined in the alloy with 5 ppm P relative to the alloy with no added phosphorous.

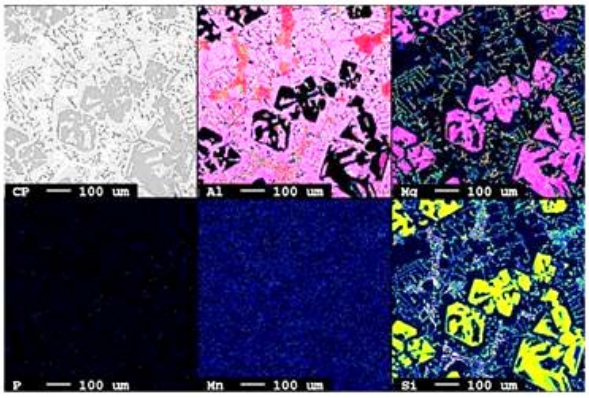

Figure 58: EPMA analysis of the base alloy with no P added, showing the backscatter electron image, and relative concentrations of Al, Mg, P, Mn and Si.

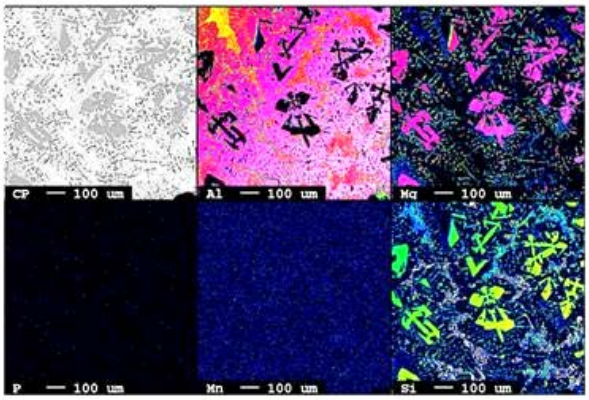

Figure 59: EPMA analysis of the alloy with 5 ppm P, showing the backscatter electron image, and relative concentrations of Al, Mg, P, Mn and Si.

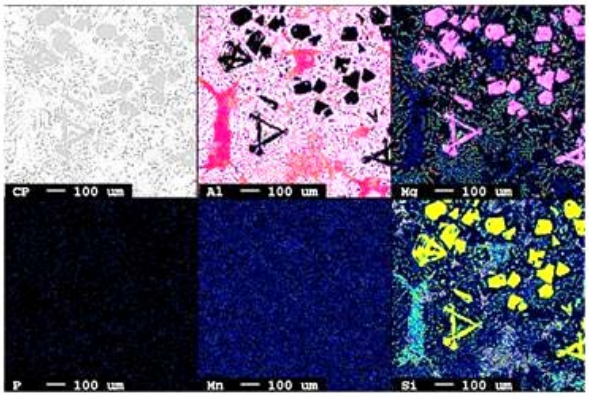

Figure 60: EPMA analysis of the alloy with 100 ppm P, showing the backscatter electron image, and relative concentrations of Al, Mg, P, Mn and Si.

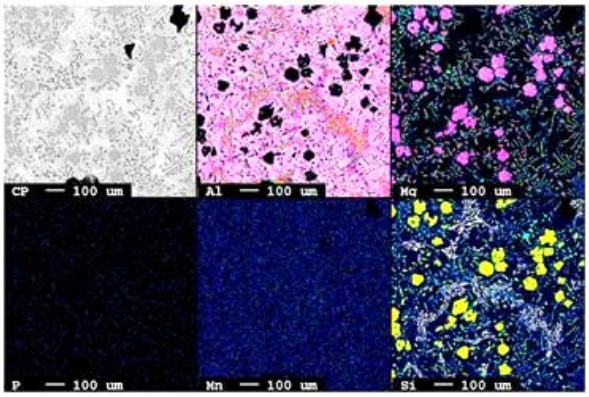

Figure 61: EPMA analysis of the alloy with 500 ppm P, showing the backscatter electron image, and relative concentrations of Al, Mg, P, Mn and Si.

Figure 62 - Figure 65 show higher magnification element maps of Al, Mg, P, Mn, Si, Cu, Fe and O in the alloys with 20 to 80 ppm added phosphorous. The element maps are recorded close to the top of the specimens, over areas containing several polygonal primary Mg_2Si particles. In all the images higher phosphorous concentrations can be observed in positions corresponding to the polygonal Mg_2Si particles. The oxygen concentration is high on the Mg_2Si particles, indicating that they oxidize easily during

sample preparation. In the alloy with 80 ppm added P a clear phosphorous enrichment is observed in the lower left corner of the element map. The same position is also enriched in oxygen, indicating that the P-rich phase on the specimen surface is oxidized. Some small needle-shaped areas rich in Fe is observed in the alloys with 20, 40 and 60 ppm added P.

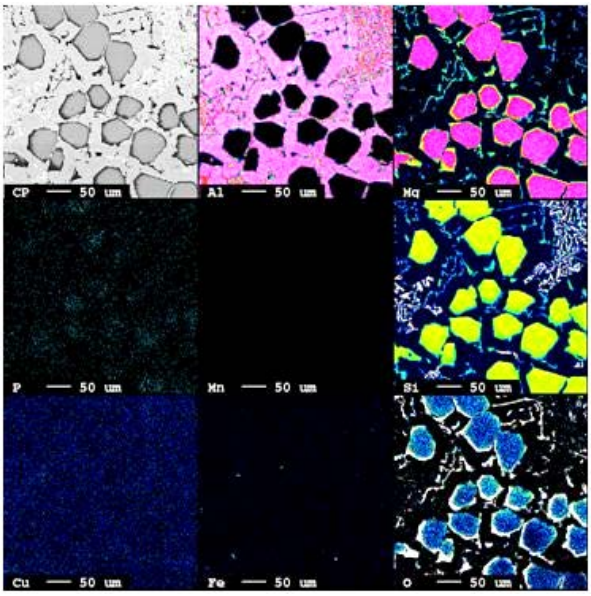

Figure 62: EPMA analysis of the primary Mg_2Si particles in the alloy with 20 ppm P, showing the backscatter electron image, and relative concentrations of Al, Mg, P, Mn, Si, Cu, Fe and O.

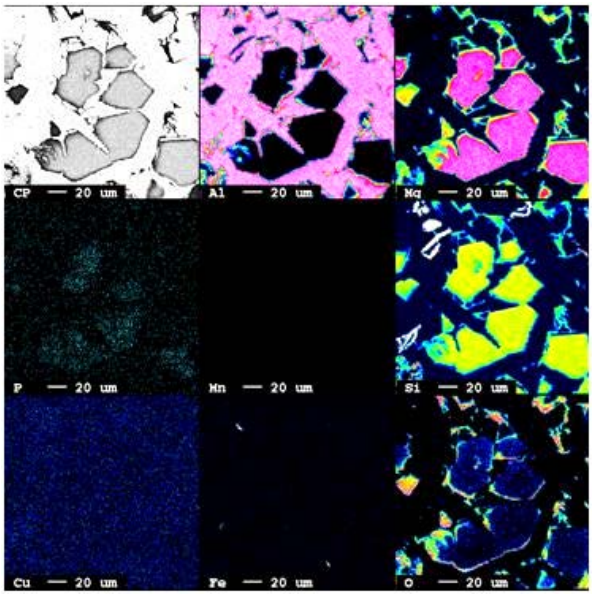

Figure 63: EPMA analysis of the primary Mg_2Si particles in the alloy with 40 ppm P, showing the backscatter electron image, and relative concentrations of Al, Mg, P, Mn, Si, Cu, Fe and O.

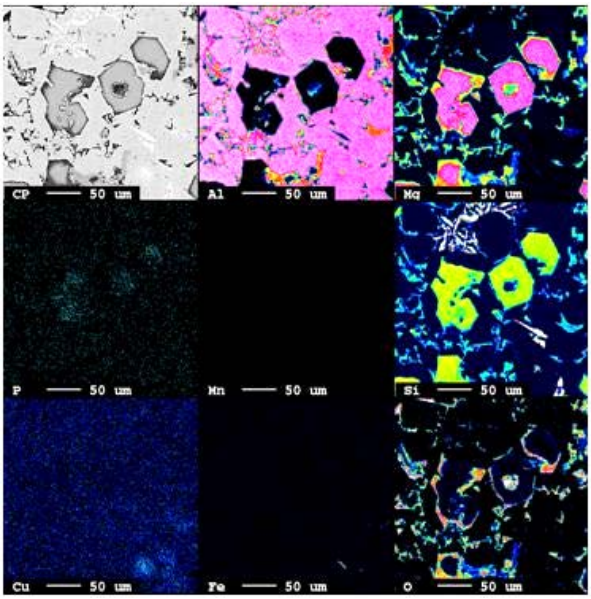

Figure 64: EPMA analysis of the primary Mg_2Si particles in the alloy with 60 ppm P, showing the backscatter electron image, and relative concentrations of Al, Mg, P, Mn, Si, Cu, Fe and O.

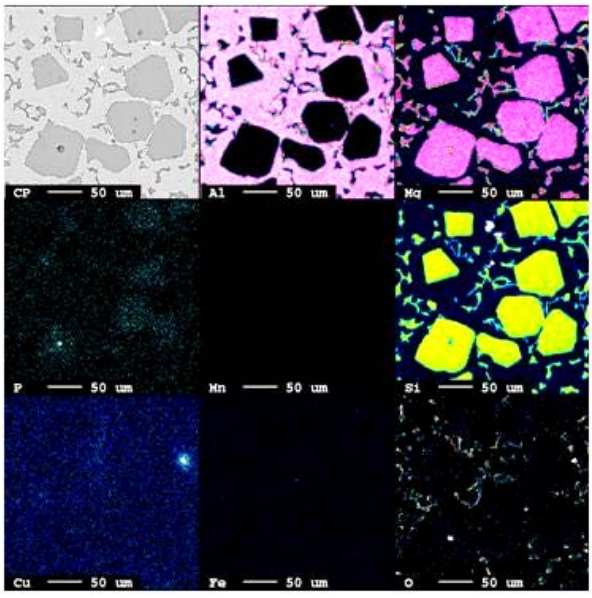

Figure 65: EPMA analysis of the primary Mg_2Si particles in the alloy with 80 ppm P, showing the backscatter electron image, and relative concentrations of Al, Mg, P, Mn, Si, Cu, Fe and O.

Figure 66 - Figure 69 show element maps of Al, Mg, P, Mn, Si, Cu, Fe and O in the alloys with 20 to 80 ppm added phosphorous. The element maps are recorded approximately 5 mm from the bottom of the specimens, over areas containing mainly binary and ternary eutectic structures. The binary Al-Mg_2Si eutectic is seen as an enrichment of Mg and Si separated by only Al. The irregular binary eutectic is separated by areas with an irregular ternary Al-Mg_2Si-Si eutectic. As can be seen in the element maps, the ternary eutectic contains only very little Mg. In the element maps of the alloys containing 60 and 80 ppm P enrichment in Cu in areas corresponding to the ternary eutectic can be observed. Some small Fe rich particles are observed in the alloys with 20, 40 and 60 ppm P.

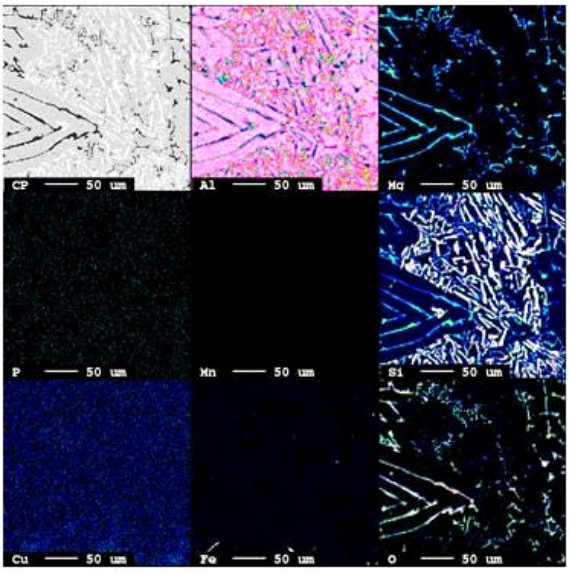

Figure 66: EPMA analysis of the eutectic structure in the alloy with 20 ppm P, showing the backscatter electron image, and relative concentrations of Al, Mg, P, Mn, Si, Cu, Fe and O.

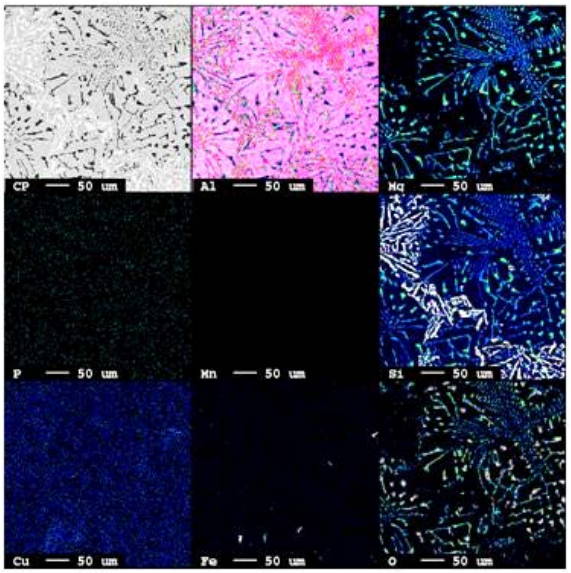

Figure 67: EPMA analysis of the eutectic structure in the alloy with 40 ppm P, showing the backscatter electron image, and relative concentrations of Al, Mg, P, Mn, Si, Cu, Fe and O.

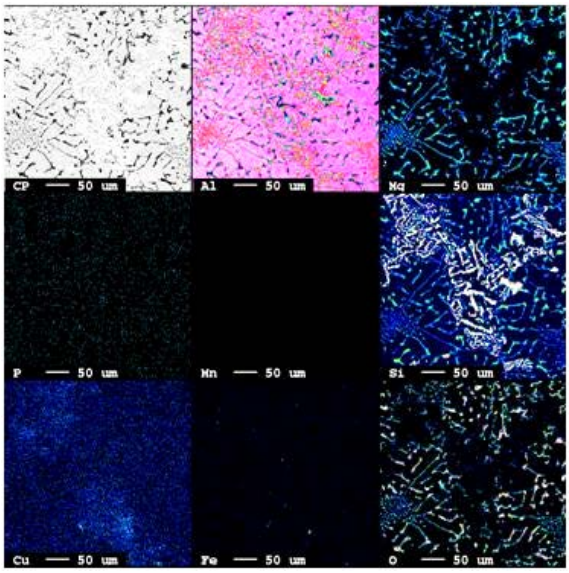

Figure 68: EPMA analysis of the eutectic structure in the alloy with 60 ppm P, showing the backscatter electron image, and relative concentrations of Al, Mg, P, Mn, Si, Cu, Fe and O.

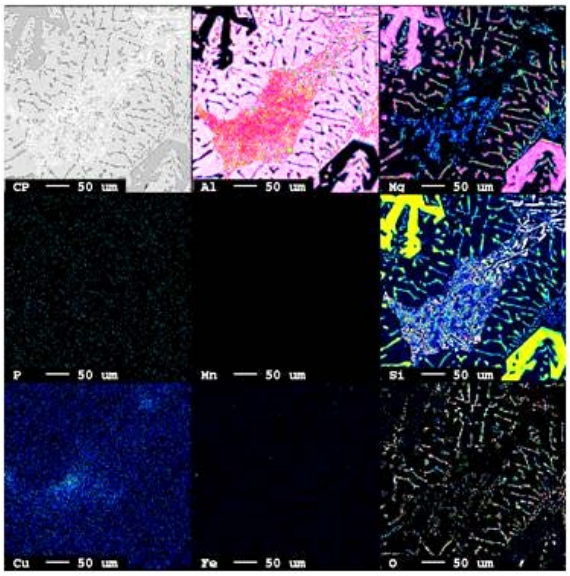

Figure 69: EPMA analysis of the eutectic structure in the alloy with 80 ppm P, showing the backscatter electron image, and relative concentrations of Al, Mg, P, Mn, Si, Cu, Fe and O.

Figure 70 shows the element maps of Al, Mg, Si, P and O over two polygonal Mg_2Si particles in the alloy with 40 and 80 ppm added phosphorous respectively. In the top image series, no particle is visible in backscattered electron mode, but an interior enrichment in P is visible. The observed particle in the lower backscattered electron image corresponds to an enrichment in Al and P relative to the surrounding area of Mg and Si.

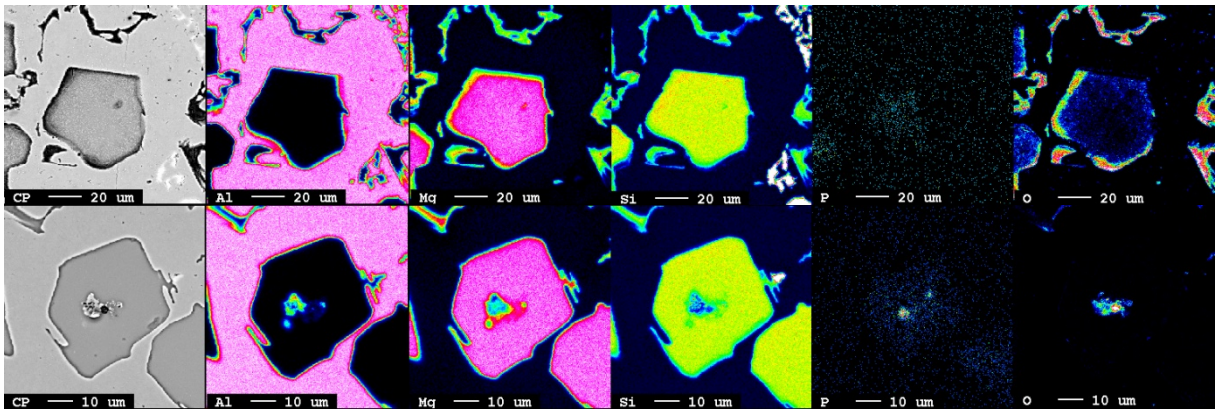

Figure 70: EPMA analysis of the two polygonal Mg_2Si particles in the alloy with 40 ppm P (upper series) and 80 ppm P (lower series) respectively, showing the backscatter electron images, and relative concentrations of Al, Mg, Si, P and O. There is an enrichment of P in the interior of both Mg_2Si particles. Where the particle is visible on the surface (lower series), the P enrichment is accompanied by an Al enrichment.

4.3.2 Chemical composition of the test alloys

The chemical composition of the test alloys are given in Table 6. Optical emission spectrometry (OES) was used to determine the Mg and Si concentrations. The concentrations of P, Ca, Fe and Cu in the alloys are determined by glow discharge mass spectrometry (GDMS). The measured Si concentrations varied between 8.6 wt% and 10.5 wt%. However, the *ALALMG* program used for quantification is only calibrated for Si contents up to approximately 2 wt% and the measurement uncertainty is therefore high. The yield of silicon additions to aluminium is usually very high and it is likely that the real silicon concentrations are closer to the target value of 10.49 wt% than the concentrations shown in Table 6. The Mg content is 0.5 - 1.5 wt% higher than the target composition of 9.51 wt%. The Mg measurements are consistent within the given measurement uncertainty of 5 %.

The alloy without added phosphorous contained 0.9 ppm P. It is clear that the efficiency of the phosphorous addition is highest for the alloys with low phosphorous content. In the alloys with nominal P content of 100 and 500 ppm the yield is only 34 and 46 ppm respectively. However, the Cu content is very consistent with the added amount of the Al-Cu-P master alloy. The concentration of Cu in the alloy without added phosphorous was 3.1 ppm, and it increases proportionally with increasing nominal P content. The Ca concentration in the samples was between 16 and 27 ppm and the Fe concentration varied between 25 and 166 ppm.

Table 6: Chemical composition of the test alloys. The Mg and Si concentrations are analyzed with OES at Hydro Aluminium Sunndalsøra. The measurement uncertainty for Mg is given as 5% of the measured value. The measurement uncertainty for Si is relatively high as the *ALALMG* program is only calibrated for Si contents up to approximately 2 wt%. Trace element concentrations of P, Ca, Fe and Cu were analyzed with GDMS. The measurement uncertainty for the GDMS results is within 10 % of the measured value.

Nominal P content	Mg [wt%]	Si [wt%]	P [ppm]	Ca [ppm]	Fe [ppm]	Cu [ppm]
0 ppm	10.1	8.6	0.9	19	166	3.1
5 ppm	10.2	8.8	4.5	17	85	55
20 ppm	10.6	9.1	13	18	79	188
40 ppm	11.1	9.5	24	16	114	364
60 ppm	11.0	10.5	31	18	40	524
80 ppm	11.0	10.4	44	22	25	748
100 ppm	10.2	9.1	34	27	75	850
500 ppm	10.6	10.3	46	19	93	4130

5 Discussion

5.1 Heterogeneous nucleating role of AlP particles

Li et al. demonstrated the inherit limitation of the Turnbull-Vonnegut equation for the case of Mg_2Si nucleating on AlP particles. They calculated the disregistry value between possible coherent interfaces of AlP and Mg_2Si crystals by including the differences in crystal structure. The crystal structures of AlP and Mg_2Si are shown in Figure 71 and Figure 72 respectively. The disregistry between the (220) plane in AlP and the (311) plane in Mg_2Si is 6.58 %, and is therefore a much better candidate for heterogeneously nucleating Mg_2Si than the cubic planes [36].

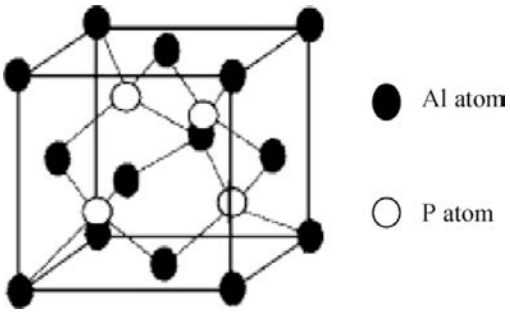

Figure 71: Zinc-blende crystal structure of AlP. Adapted from Fig. 5 [36].

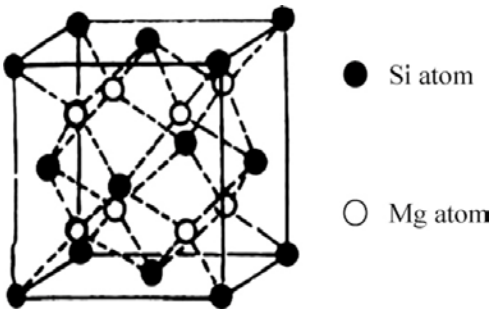

Figure 72: Fluorite crystal structure of Mg_2Si. Adapted from Fig. 6 [36].

Lescuyer et al. studied solubility and precipitation of AlP in Al-Si melts by a temperature controlled filtration technique [40]. The recent model by Liang and Schmid-Fetzer [39] shows good agreement with the experimental data published by Lescuyer et al. By studying the size distributions of the AlP particles at 800 °C they found the particle size to be approximately symmetrically distributed around a mean size of around 5 µm as shown in Figure 73. In this work the AlP particles observed by EPMA analysis had diameters ranging from 3 µm to 10 µm, and the size is assumed to be approximately normally distributed around a mean size of 5 µm. This is a reasonable assumption as the AlP particle size is the result of a continuous precipitation, growth and dissolution process approaching dynamic equilibrium [37].

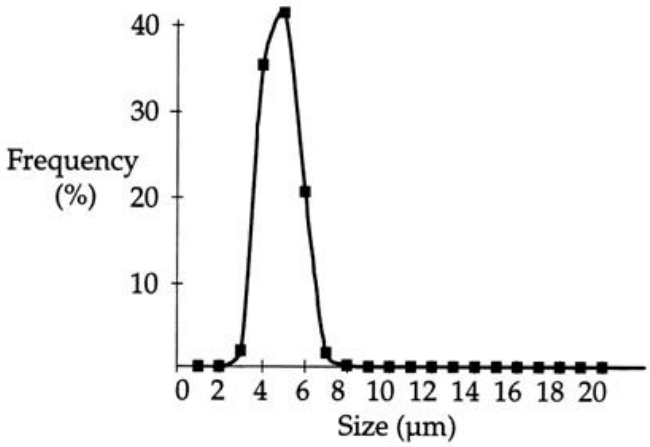

Figure 73: AlP particle size distribution at 800 °C determined by a temperature controlled filtration technique by Lescuyer et al. The figure is adapted from Fig. 9 [40].

By assuming that all added phosphorous is in the form of AlP particles built up by Al_6P units, it is possible to calculate the number of AlP particles present in the melt. The particles are assumed to be cubic of average size 5 µm. By using the density for AlP described by Wang and Zaheeruddin of 2.40 g · cm^{-3} [48], and approximating the melt density by the rule of mixtures to be 2.32 g · cm^{-3} the number density of AlP particles can be found. The results are given in Table 7, with the detailed calculations given in Appendix 3.

Table 7: Calculated amount of AlP particles, and measured area number density of primary Mg_2Si particles converted to volumetric number density by accounting for average primary particle size. The detailed calculations of the amount of AlP particles are given in Appendix 3.

Phosphorous concentration	**AlP particles · mm^{-3}**	**Number density Primary Mg_2Si**
5 ppm	241	10-20 particles · mm^{-3}
20 ppm	965	600 particles · mm^{-3}
40 ppm	1930	837 particles · mm^{-3}
60 ppm	2896	958 particles · mm^{-3}
80 ppm	3860	895 particles · mm^{-3}
100 ppm	4825	915 particles · mm^{-3}

To convert the area number density of primary Mg_2Si particles to volumetric number density, the particle size has to be taken into account. Figure 74 illustrates the principle; the three particles on the right hand side are visible in the micrograph, while the left particle is not. The volumetric number density is then calculated by dividing the area number density by the average particle size (h).

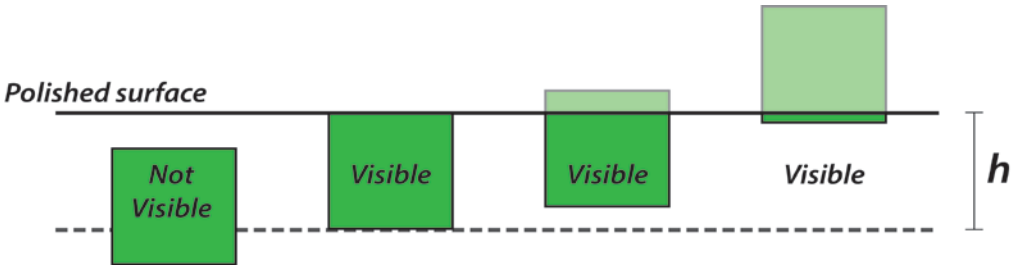

Figure 74: Method of transforming the area number density to the volumetric number density. The particle to the left is not visible in the micrograph, while the three others are. The average particle size is given as *h*.

To describe the nucleating potential of AlP, the theoretically calculated amount of AlP particles present in the melt per unit volume and the volumetric number densities of primary Mg_2Si particles found from the micrographs were compared. It is clear that addition of 5 ppm phosphorous is not sufficient to effectively nucleate primary Mg_2Si particles. This might be because the real number of AlP particles in the melt is smaller than the theoretically calculated number. Phosphorous can have oxidized, reacted with other impurity elements in the melt or be dissolved in the melt. For the alloys with 20 and 40 ppm added P, nucleation seems to occur on most of the AlP particles present in the melt. Even for potent inoculating particles such as TiB_2 in aluminium, nucleation only occurs on a fraction of the substrate particles. It is therefore reasonable to assume that nucleation occurred on all the favorable particles in these two alloys, leading to site saturation.

The alloys with 60, 80 and 100 ppm added P do not show a further increase in the number of nucleated primary Mg_2Si particles. This is explained by nucleation rapidly occurring on all favorable AlP particles, causing a recalescence due to the release of latent heat. The undercooling is decreased, retarding further nucleation on the smaller remaining AlP particles in the melt. Upon further cooling, solidification is likely to proceed mainly by the growth of the already nucleated Mg_2Si particles. Moreover, AlP particles can agglomerate in the melt if the melt is not stirred. However, as the melt was properly stirred before filling the steel die, this is not expected to have influenced the results.

To clarify the importance of the AlP substrate particle size, the free-growth model (presented in section 2.1) was applied to the nucleation of Mg_2Si particles. The solid-liquid surface energy for Mg_2Si is not well studied in the literature. Liao et al. found that the surface energy of Mg_2Si decreases with increasing concentration of Mg relative

to Si [49]. Thus, it is reasonable to assume that the solid-liquid surface energy of Mg_2Si in Al-Mg-Si melts lies between the value for Si in an Al-20% Si melt of 0.4107 $J \cdot m^{-2}$, as studied by Jian et al. for the case of an Al-Si alloy at 850 K [50], and a pure Al melt (0.167 $J \cdot m^{-2}$) as studied in previous studies by the same authors [51]. The values used for the calculations are given in Table 8.

Table 8: Properties used for calculating the free growth undercooling for primary Mg_2Si as a function of substrate particle size. (* The solid-liquid surface energy is an assumed value)

Property	Value
Entropy of fusion (ΔS_f)	22 [$J \cdot g^{-1} \cdot atom^{-1} \cdot K^{-1}$] [10]
Solid-liquid surface energy (σ_{sl})	0.30 [$J \cdot m^{-2}$] * [49-51]
Molar mass ($M_{(Mg_2Si)}$)	76.70 [$g \cdot mol^{-1}$] [52, p. 3-1]
Density (ρ)	$1.990 \cdot 10^6$ [$g \cdot m^{-3}$] [1]

Figure 75 shows the calculated free growth undercooling as a function of AlP particle diameter. For small particles, very high undercoolings are required for free growth. For a particle diameter of 5 µm an undercooling of 0.14 K is required for free growth. For a particle diameter of 1 µm an undercooling of 0.70 K is required, and the undercooling increases rapidly with decreasing particle size below this.

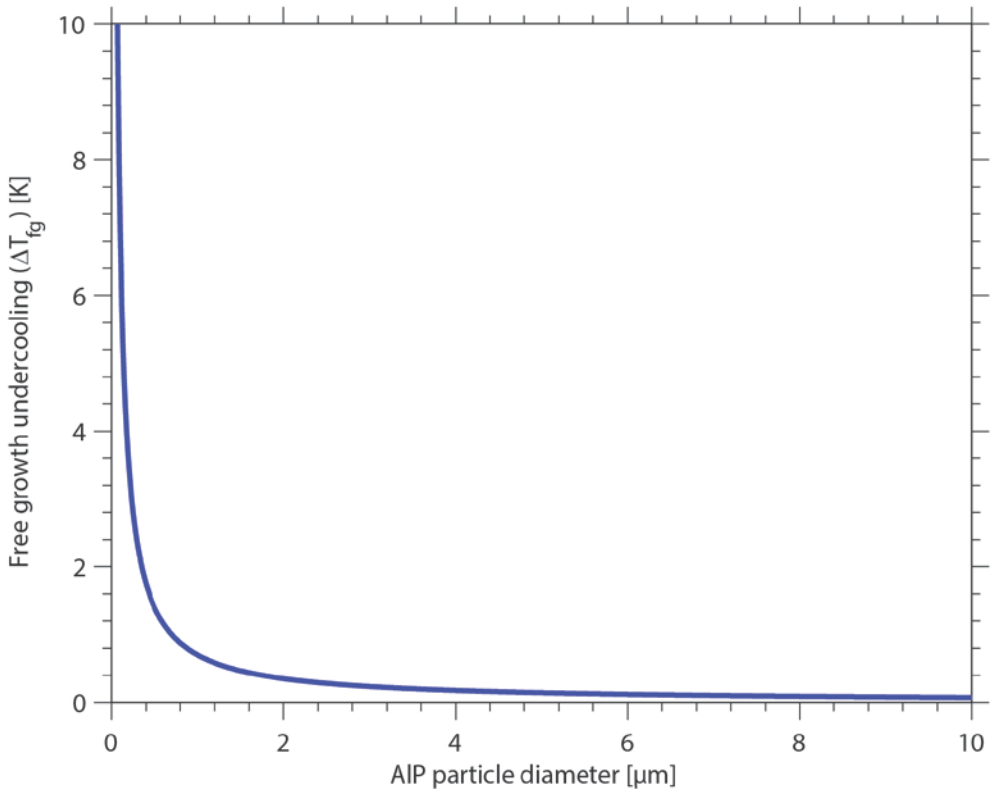

Figure 75: Calculated free growth undercooling as a function of AlP substrate particle diameter.

The measured nucleation temperatures for the primary Mg_2Si reactions vary with phosphorous addition. It rapidly increases from 640.6 °C without added P to 656.4 °C with 20 ppm added P. However, the measured temperatures are not in agreement with the liquidus temperature in the phase diagram of 628.0 °C for the nominal alloy composition. Nucleation is not expected to occur above the liquidus temperature. The equilibrium liquidus temperature increases with increasing Mg content, and a liquidus temperature as measured here, corresponds to an alloy with approximately 20 wt% Mg_2Si.

This deviation is explained by the produced alloys being higher in Mg than the nominal alloy composition. The OES measurements show that the resulting Mg content was between 10.1 wt% and 11.1 wt% compared to the nominal Mg content of 9.51 wt%. The real oxidation loss of Mg during alloy preparation was approximately 10 %, compared to the assumed 20 %. Moreover, the measured nucleation temperatures for the binary eutectic reaction are in the range of 584 - 585 °C compared to the equilibrium binary eutectic temperature of 582.3 °C for the nominal alloy composition. The raised binary eutectic temperature is also explained by a higher Mg content than the nominal composition. In addition, the effect of phosphorous on the Al-Mg-Si ternary phase diagram is not well studied, and it is possible that phosphorous addition affects the phase equilibria and thus changes the phase diagram.

As shown in Figure 75, the free growth undercooling for the assumed average AlP particle size is 0.14 K. By assuming that this is correct for the alloys with the highest nucleation temperatures (i.e. least resistance to nucleation) the real liquidus temperature for these alloys should be approximately 656.5 °C.

5.2 Effect of phosphorous on the primary Mg_2Si particle morphology

Mg_2Si exhibits faceted growth morphologies, which is common for non-metals and intermetallic compounds. Faceted growth occurs due to limitations in the kinetics of atom attachment to the interface. Generally, atoms attach more easily to the inherently rough, high-index planes than the low-index planes [20, pp. 34-35]. The resulting crystal shape is determined by the slowest growing planes. Jackson's factor (α), which is the dimensionless entropy of fusion, gives a good indication of the growth morphology as it reflects the difference between the solid phase and the liquid phase [53].

The growth rate will vary in different crystallographic directions if the surface energy is anisotropic. This was treated theoretically by Jackson, who calculated growth rate coefficients (K_{hkl}) for different crystallographic planes for the case of a simple cubic two-dimensional crystal [54]. The growth rate of a crystallographic plane (V_{hkl}) is related to the undercooling (ΔT) and the growth rate coefficient by Equation 6, which is valid for small undercoolings [20, p. 40].

$$V_{hkl} = K_{hkl} \cdot \Delta T \qquad \textit{(Eq. 6.)}$$

Wang, Lu et al. demonstrated that the ratio of the growth rate in the <100> (V_{100}) and <111> (V_{111}) directions determine the resulting crystal morphology for primary Si [30]. This idea was further applied to primary Mg_2Si by Li et al [28]. They argued that $V_{100}/V_{111} = \sqrt{3}$ will lead to an octahedral morphology, $V_{100}/V_{111} = \sqrt{3}/3$ will lead to a cubic morphology and values between these two outer cases will lead to a truncated octahedron (Figure 76).

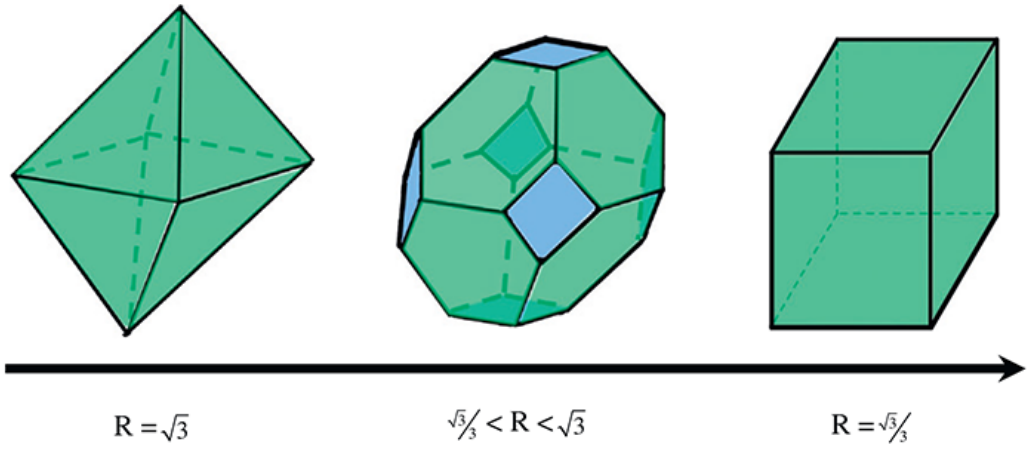

Figure 76: The different morphologies of Mg_2Si resulting from different ratios between the growth rate in the <100> and <111> directions (R = V_{100}/V_{111}). The figure is adapted from Fig. 9 [28].

More phosphorous introduces more heterogeneous nucleation sites, and nucleation occurs at lower undercoolings. Lower undercoolings lead to lower growth rate as indicated by Equation 6. As the number of nucleated primary Mg_2Si particles increase with increasing phosphorous content, more latent heat will be released. Simultaneously, the supersaturation of Mg and Si in the melt decreases rapidly as the particles are nucleated. Both these factors contribute to a decreased driving force for growth. It is possible that this initial, slow growth allows for the formation of a boundary layer enriched in aluminium surrounding the growing particles, retarding further growth of

Mg_2Si. Aluminium accumulates in front of the {111} planes, while the <100> directions, in comparison, have access to a larger volume of melt, and therefore grows faster. This leads to the formation of octahedral crystals. If the aluminium enrichment is even higher in the melt due to many Mg_2Si particles having nucleated, it is possible that growth in the <100> directions will also be retarded. This would explain the truncated octahedron or tetrakaidecahedron particles observed in the alloys with the highest phosphorous contents.

In the thermal analysis, a secondary peak in the primary crystallization field of Mg_2Si is observed for the alloys with 5, 20 and 40 ppm added phosphorous. The temperature range of this secondary reaction decreases from 635 °C - 620 °C for 5 ppm P, to 612 °C – 595 °C for 20 ppm P and 605 °C - 584 °C for 40 ppm P. The high nucleation temperature for the primary reaction peak is a result of heterogeneous nucleation at favorable AlP particles. As discussed above, a higher phosphorous content leads to more AlP particles in the melt and more Mg and Si consumed in nucleating and growing primary Mg_2Si particles on these inoculating particles.

The secondary reaction peak is due to nucleation of primary Mg_2Si particles on either smaller AlP particles, other particles present in the melt or oxide particles. The nucleation at these sites proceeds at higher undercoolings, leading to a high initial growth rate and a dendritic morphology. In the alloys with low phosphorous content, nucleation rapidly occurs on all favorable AlP particles, leading to site saturation. Solidification can only proceed by further growth of these nucleated particles until either the undercooling is high enough so that other heterogeneous nucleation sites become favorable, or more AlP particles are precipitated as the solubility decreases. For phosphorous contents of 60 ppm or higher, enough AlP particles are present in the melt to avoid site saturation, which is further supported by the fraction of polygonal primary Mg_2Si particles of 98 %.

The primary particle sizes and morphologies observed in the present work are in good agreement with previously published results by other authors. However, little research has been done on very pure alloys, as studied here. The phosphorous contents studied in the literature is typically 0.1 – 1.0 wt% P. Tebib et al. reported a morphology modification of primary Mg_2Si from coarse dendritic to polygonal with refinement in size from 300 µm to 60 µm with addition of 0.4 wt% P to an Al-15Si-14Mg-4.6Cu alloy

[33]. Qin et al. reported a similar modification and refinement from 300 μm to 20 μm with the addition of 0.454 wt% P to an Al-25Mg_2Si-3Si-3Cu alloy. It seems that more phosphorous is needed for effective modification in alloys with higher impurity concentrations [10]. This is expected as phosphorous can form other compounds which are less favorable as heterogeneous nucleation sites than AlP.

5.3 Effect of phosphorous addition on the eutectic structures

In the literature, phosphorous concentrations as high as 0.4 wt% have been reported not to have a significant influence on the eutectic structures [33]. This corresponds well with the present study as no clear microstructural changes are observed with increasing phosphorous content. However, there are some observed effects in the thermal analysis. The nucleation temperature for the binary eutectic reaction is approximately 2.5 °C higher in the alloy without P addition than the remaining alloys. In addition, the characteristic temperatures for the ternary eutectic reaction are approximately 2.5 °C lower in the sample with 500 ppm P compared to the sample with 100 ppm P. There is an observed declining trend in these characteristic temperatures with increasing phosphorous content.

The unmodified alloy requires a higher undercooling for the primary Mg_2Si reaction, and fewer primary particles are formed. This can lead to the melt being richer in Mg and Si at the eutectic temperature relative to the alloys modified with phosphorous. The melt composition affects the binary eutectic temperature, represented by the e_3 line in the Al corner of the Al-Mg-Si ternary phase diagram (Figure 77). As discussed previously, the resulting Mg contents in the alloys were 0.5 – 1.5 wt% higher than the target alloy composition, due to less oxidation than assumed during alloy preparation. According to the phase diagram, the binary eutectic temperature increases with increasing Mg content. However, this is observed in all the alloys and will thus raise all the binary eutectic temperatures correspondingly.

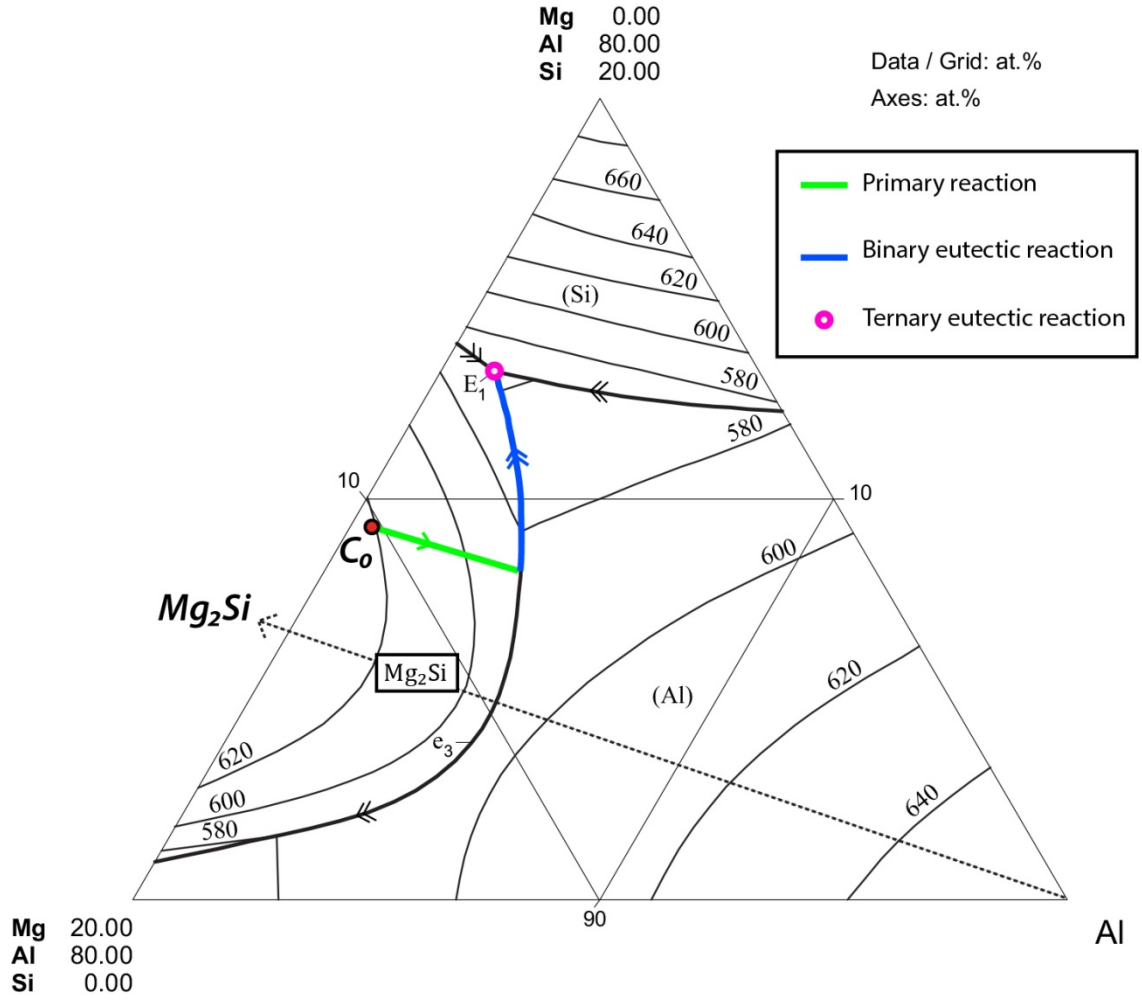

Figure 77: Liquidus projection of the Al-rich corner of the Al-Mg-Si ternary phase diagram. The equilibrium solidification path from the alloy concentration is illustrated. The axes and grid are in at%, with the nominal alloy composition (C_0) 79.50 at% Al, 10.48 at% Mg and 10.02 at% Si. The maximum temperature for the binary eutectic reaction is 594 °C, located where the e_3 line intersects the dotted Al-Mg_2Si alkemade line. Adapted from Fig. 4 [55].

Although the characteristic temperatures for the ternary eutectic reaction are found to decrease with increasing phosphorous content, this effect is not likely to be an attribute of the phosphorous content or aluminium phosphide particles. It should be remembered that phosphorous is added through an Al-19Cu-1.4P master alloy, resulting in a nominal copper concentration of 0.68 wt% in the alloy with 500 ppm added P. It has previously been argued that Cu addition should change the eutectic temperature in Al-Mg_2Si alloys [10], and Moustafa et al. found that Cu lowers the eutectic temperature in Al-Si alloys [56].

From the EPMA element maps of the cast specimens it is clear that the ternary eutectic contains very little Mg, consisting mainly of Al and Si. Therefore the results of Moustafa

et al. should be applicable also to the ternary eutectic phase in the test alloys studied in the present work. Figure 78 shows the calculated quasi-binary (Al-15Mg_2Si-5Si) – Cu phase diagram. It is clear that the primary Mg_2Si reaction, the binary Al-Mg_2Si eutectic reaction and the ternary Al-Mg_2Si-Si eutectic reaction temperatures all decrease with increasing Cu content. The ternary eutectic temperature is decreased from 557 °C without Cu to 555.2 °C with 0.68 wt% Cu. This corresponds well to the measured decrease in nucleation temperature from 550.1 °C in the base alloy to 547.2 °C in the alloy with 0.68 wt% added Cu through the master alloy.

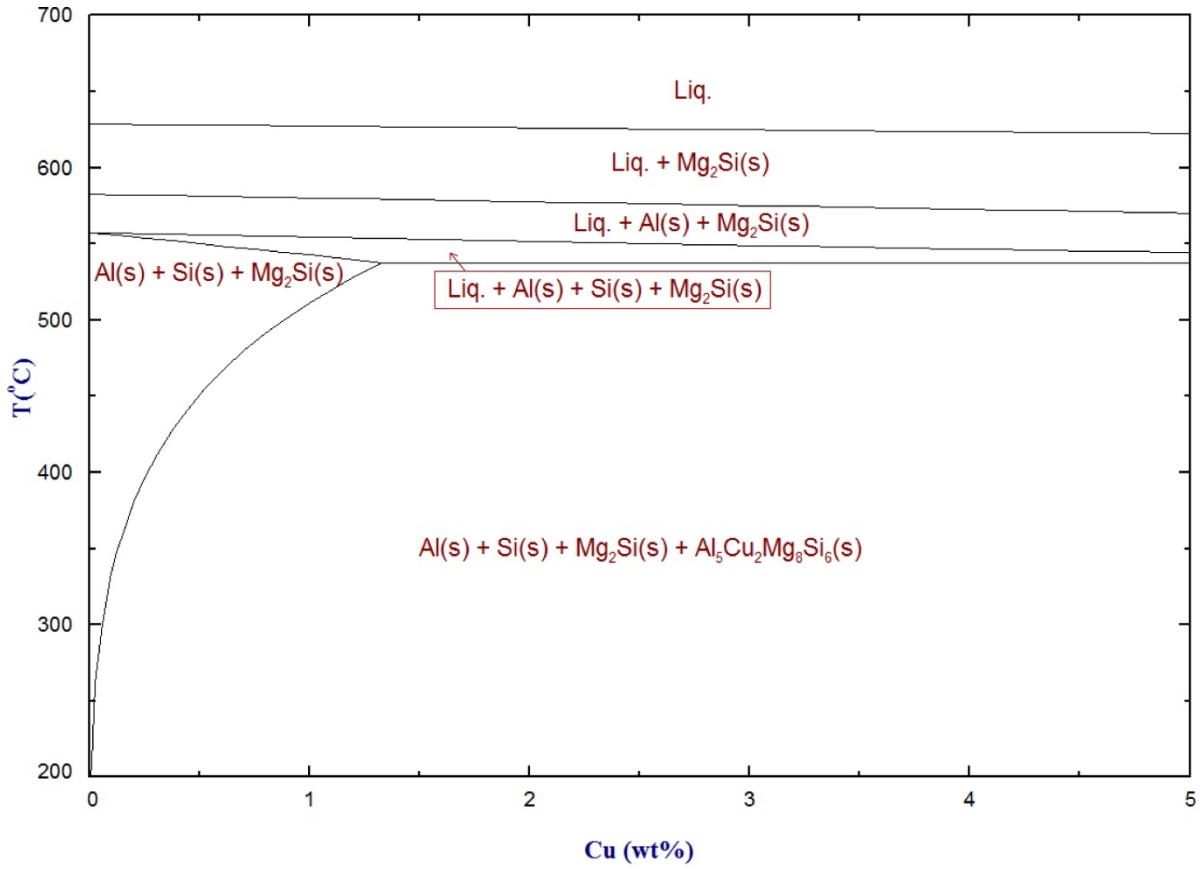

Figure 78: Quasi-binary phase diagram of (Al-15Mg_2Si-5Si) – Cu calculated by FactSage 6.4. The ThermoTech Al database version 3.0 was used for the calculations. It is clear that the primary, binary eutectic and ternary eutectic reaction temperatures all decrease with increasing Cu content.

Copper has been found to have low solid solubility in Al-Mg-Si alloys and segregate strongly to the intercellular regions in the eutectic structures, as can also be seen in the EPMA element maps of these structures (Figure 66 - Figure 69). In areas enriched with Cu, hard Cu-rich intermetallics such as θ-phase (Cu_2Al) and Q-phase (quaternary Al-Mg-Si-Cu phase) can be formed. These contribute positively to the strength, but can have adverse effects on ductility.

5.4 Effect of macrosegregation and gas porosity on the microstructure

There are several mechanisms that can lead to macrosegregation in castings, most of which involve transport of enriched liquid in the mushy zone. The topic of macrosegregation in aluminium castings was reviewed by Eskin and Katgerman [57]. In the present study, the severe macrosegregation of the precipitated primary Mg_2Si particles is of importance. The two main mechanisms leading to macrosegregation of primary Mg_2Si particles are likely to be:

- ***Transport of precipitated particles in the melt by buoyancy forces.*** The density of Mg_2Si is 1.99 $g \cdot cm^{-3}$ compared to the average density of the melt which is approximately 2.3 $g \cdot cm^{-3}$ at the liquidus temperature.

- ***Forced melt flow caused by melt pouring or gas evolution during solidification.*** In the present work, gas evolution is likely to have affected macrosegregation of primary Mg_2Si particles, as gas bubbles formed early in the solidification will rise towards the top of the casting, inducing a melt flow. This principle is illustrated in Figure 79.

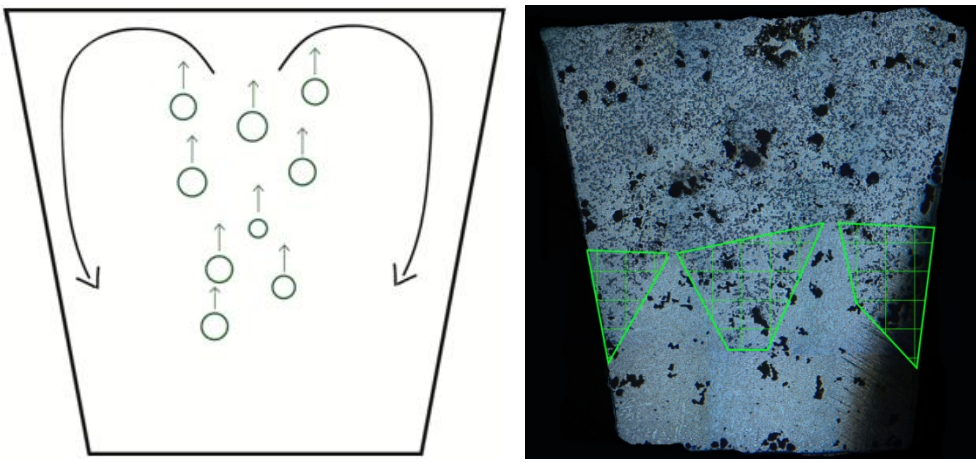

Figure 79: Schematic drawing of the melt flow caused by gas bubbles rising towards the top of the casting (left), next to the macroscopic image of the specimen with 20 ppm added phosphorous (right). The dark grey primary Mg_2Si particles appear further down in the cast specimen along the side walls and in the center as indicated by the green square grid areas.

For industrial applications the melt would have had to be degassed before casting. Al-15Mg_2Si-5Si alloys have generally good castability, and as Si expands upon solidification little or no porosity is expected if the melt is degassed prior to solidification. Without gas pores forming during solidification the forced melt flow will not be present to the same extent. The buoyancy-driven macrosegregation is however not as easy to avoid.

As was seen in Figure 14, the primary Mg_2Si particles have a larger tendency towards macrosegregation in the alloys with high phosphorous concentrations. This is attributed to the morphology modification associated with the phosphorous addition. The smaller polygonal Mg_2Si particles easily agglomerate at the top of the cast specimen, while the large dendritic Mg_2Si particles observed in the specimens with 0 and 5 ppm added phosphorous become coherent and stifle movement. As polygonal Mg_2Si particles are the preferred morphology, measures to reduce macrosegregation for these alloys have to be taken. Macrosegregation can be reduced by applying electromagnetic stirring during casting [58]. However, this is mainly applicable for continuous cast sections or sections with simple geometries. As buoyancy-driven macrosegregation is a time dependent process, another possibility is to increase the cooling rate during solidification. This will increase the tendency of dendritic growth, thus requiring a higher level of phosphorous (or addition of another modifying element) to maintain the polygonal morphology of primary Mg_2Si.

Macrosegregation of the primary Mg_2Si particles can also be used as an advantage for cast components. With the proper choice of a casting process, more wear resisting particles can be present in certain areas of the casting. This is of interest in for example brake disks, where a larger number of reinforcing particles close to the circumference is positive. The outer radius of the brake disks moves faster relative to inner, resulting in higher potential wear which can be counteracted by the increased number of reinforcing particles.

5.5 Further work and future possibilities

This project has been concerned with the solidification behavior of Al-15Mg_2Si-5Si alloys with added phosphorous cast in steel dies through common gravity casting. There are several possibilities of taking this work further in future projects. The most obvious is to examine the alloys during directional solidification. By this technique the solidification parameters G (temperature gradient) and V (growth rate) can be controlled independently. The effects of these parameters on the microstructural characteristics can be determined, providing better insight as to how these alloys should be solidified for optimal properties.

As the Department of Materials Science and Engineering together with the Department of Physics are working on in situ imaging of directionally solidified alloys by the use of

X-rays, the possibility of further examining the nucleation and growth mechanisms of primary Mg_2Si particles exists. This could further develop on the growth mechanisms discussed in the present work, as well as examining the effect of other elements.

The present work has studied the effects of phosphorous additions in high purity alloys. As industrial processes never will be concerned with such pure alloys, the effects of other elements on the modification effect of phosphorous should be studied. Research by other authors has shown that much higher phosphorous additions are necessary for effective modification in commercial purity alloys. Therefore, determining which elements that reduce the effect of phosphorous is of interest.

A more practical approach is also possible. The interest in MMCs is growing in the industry, but the use of these alloys is limited by challenges in the casting processes. To optimize the alloy and casting process for a specific product in cooperation with a foundry, would be an interesting project with a hands-on approach.

6 Conclusions

The solidification behavior of Al-15Mg_2Si-5Si alloys with phosphorous contents from 0 to 500 ppm was studied by thermal analysis and microstructural examinations. The main focus of the work was on nucleation of primary Mg_2Si particles.

It was found that:

- By addition of 500 ppm phosphorous, the morphology of the primary Mg_2Si particles is modified from coarse dendrites to fine polygonal particles. The average size of these particles is reduced from 112 µm to 43 µm. 5 ppm phosphorous significantly refines the size of the primary Mg_2Si particles, but is not sufficient to effectively modify the morphology. With addition of 60 ppm phosphorous, 98 % of the primary Mg_2Si particles have a polygonal morphology.

- The number of nucleated primary Mg_2Si particles increases with increasing phosphorous addition up to 60 ppm, but does not increase further with higher additions. This is attributed to the recalescence reducing the initial growth rate, allowing the formation of an Al-enriched boundary layer and thus retarding further growth of Mg_2Si.

- Various polygonal primary Mg_2Si morphologies were observed: Equiaxed dendritic, hopper crystal, octahedron, truncated octahedron and tetrakaidecahedron. The tendency for truncated octahedron and tetrakaidecahedron increases with increasing phosphorous content and is attributed to the Al-enriched boundary layer retarding growth in the <100> directions.

- The real oxidation loss of Mg was close to 10 %, compared to the assumed 20 %, and the real alloy composition was thus approximately 1 wt% higher in Mg than the target composition.

- The nucleation temperature for the primary Mg_2Si reaction increased from 640.6 °C to 651.2 °C with addition of 5 ppm P, and reached a maximum of 656.4 °C with 20 ppm P. This is attributed to heterogeneous nucleation of Mg_2Si on AlP particles.

- The observed secondary reaction peak indicates nucleation on smaller AlP particles, other particles present in the melt or oxide particles after primary Mg_2Si have nucleated on all favorable AlP particles. The nucleated Mg_2Si particles associated with the secondary reaction peak have a dendritic morphology.

- Phosphorous addition was not found to affect the binary and ternary eutectic structures. However, the master alloy contained a considerable amount of Cu, which according to the phase diagram decreases the binary and ternary eutectic temperatures.

- The cast samples showed significant macrosegregation and considerable gas porosity due to the choice of an improper casting process.

7 Acknowledgements

I wish to thank my supervisor Prof. Lars Arnberg of the Department of Materials Science and Engineering, NTNU, for providing an interesting research topic and excellent guidance through meaningful theoretical and practical discussions.

I also wish to thank PhD Thomas Hartmut Ludwig of the AMPS Team at Hydro Aluminium Årdal for introducing me to this research topic, introducing me to accurate thermal analysis and helpful theoretical discussions around the results.

I sincerely thank Prof. Yanjun Li of the Department of Materials Science and Engineering, NTNU, for taking interest in my thesis and helpful discussions around the results and possible further work.

I thank senior engineer Morten Peder Raanes at the Electron Microscopy Laboratories, Department of Materials Science and Engineering, NTNU, for assistance with chemical analysis by EPMA.

I wish to thank technical manager Thomas Jäger of Vigeland Metal Refinery AS for generous supply of high purity aluminium.

For confirmative composition measurements of Mg and Si by optical emission spectrometry I thank Principal Research Scientist Petter Åsholt at Hydro Aluminium Sunndalsøra.

I also thank Researcher Dr. Kai Tang at SINTEF Materials and Chemistry for assistance with phase diagram calculations in FactSage.

For excellent help with the experimental work by providing laboratory equipment I wish to thank senior engineer Trygve Lindahl Schanche of the Department of Materials Science and Engineering, NTNU.

Last, but not least, I thank Prof. Marisa Di Sabatino and Post doc. Chiara Modanese of the Department of Materials Science and Engineering, NTNU, for introducing me to glow discharge mass spectrometry and providing quantitative chemical analyses of my alloys.

8 References

1. Nasiri, N., et al., *Microstructure and tensile properties of cast Al-15%Mg2Si composite: Effects of phosphorous addition and heat treatment.* Materials Science and Engineering a-Structural Materials Properties Microstructure and Processing, 2012. **556**: p. 446-453.

2. *MX Composites*. [cited 2014 23.04]; Available from: http://www.mxcomposites.com/.

3. *REL, Inc.* [cited 2014 23.04]; Available from: http://www.relinc.net/adv-materials/metal-matrix-composite/.

4. Zhao, Y.G., et al., *In-situ Mg2Si/Al-Si-Cu composite modified by strontium.* Journal of Materials Science, 2005. **40**(7): p. 1831-1833.

5. Pacz, A., *Alloy*. 1921, Pacz, Aladar: United States.

6. Zhang, J., et al., *Microstructural development of Al–15wt.%Mg2Si in situ composite with mischmetal addition.* Materials Science and Engineering: A, 2000. **281**(1–2): p. 104-112.

7. Zhao, Y.G., et al., *In situ Mg2Si/Al-Si composite modified by K2TiF6.* Materials Letters, 2004. **58**(16): p. 2192-2194.

8. Hadian, R., M. Emamy, and J. Campbell, *Modification of Cast Al-Mg2Si Metal Matrix Composite by Li.* Metallurgical and Materials Transactions B-Process Metallurgy and Materials Processing Science, 2009. **40**(6): p. 822-832.

9. Emamy, M., R. Khorshidi, and A.H. Raouf, *The influence of pure Na on the microstructure and tensile properties of Al-Mg2Si metal matrix composite.* Materials Science and Engineering: A, 2011. **528**(13–14): p. 4337-4342.

10. Qin, Q.D., et al., *Effect of phosphorus on microstructure and growth manner of primary Mg2Si crystal in Mg2Si/Al composite.* Materials Science and Engineering a-Structural Materials Properties Microstructure and Processing, 2007. **447**(1-2): p. 186-191.

11. Wang, H.Y., et al., *Modification of Primary Mg2Si in Mg-4Si Alloys with Antimony.* Metallurgical and Materials Transactions a-Physical Metallurgy and Materials Science, 2012. **43A**(13): p. 4926-4932.

12. Qin, Q.D., et al., *Strontium modification and formation of cubic primary Mg2Si crystals in Mg2Si/Al composite.* Journal of Alloys and Compounds, 2008. **454**(1–2): p. 142-146.

13. Mabuchi, M., K. Kubota, and K. Higashi, *Effect of Hot Extrusion on Mechanical-Properties of a Mg-Si-Al Alloy.* Materials Letters, 1994. **19**(5-6): p. 247-250.

14. Mabuchi, M. and K. Higashi, *Strengthening mechanisms of Mg-Si alloys.* Acta Materialia, 1996. **44**(11): p. 4611-4618.

15. Riffel, M. and J. Schilz, *Mechanical Alloying of Mg2Si.* Scripta Metallurgica Et Materialia, 1995. **32**(12): p. 1951-1956.

16. Hou, J., C. Li, and X.F. Liu, *Nucleating role of an effective in situ Mg3P2 on Mg2Si in Mg-Al-Si alloys.* Journal of Alloys and Compounds, 2011. **509**(3): p. 735-739.

17. Hekmat-Ardakan, A. and F. Ajersch, *Thermodynamic evaluation of hypereutectic Al–Si (A390) alloy with addition of Mg.* Acta Materialia, 2010. **58**(9): p. 3422-3428.

18. Ludwig, T.H., *Trace elements in Al-Si foundry alloys*. Vol. 2013:360. 2013, Trondheim: Norges teknisk-naturvitenskapelige universitet.

19. Zhang, J., et al., *Microstructural evolution of the in situ Al-15wt.%Mg2Si composite with extra Si contents.* Scripta Materialia, 2000. **42**(11): p. 1101-1106.

20. Kurz, W. and D.J. Fisher, *Fundamentals of solidification*. 1998, Uetikon-Zuerich: Trans Tech Publications. 305 s. : ill.

21. Uhlmann, D.R. and B. Chalmers, *Energetics of Nucleation.* Industrial and Engineering Chemistry, 1965. **57**(9): p. 19-31.

22. Greer, L., *Control of grain size in solidification*. Solidification and Casting, ed. B. Cantor and K. Oreilly. 2003. 199-247.

23. Maxwell, I. and A. Hellawell, *Simple Model for Grain Refinement During Solidification.* Acta Metallurgica, 1975. **23**(2): p. 229-237.

24. Greer, A.L., et al., *Modelling of inoculation of metallic melts: Application to grain refinement of aluminium by Al-Ti-B.* Acta Materialia, 2000. **48**(11): p. 2823-2835.

25. Mabuchi, M., K. Kubota, and K. Higashi, *Tensile strength, ductility and fracture of magnesium-silicon alloys.* Journal of Materials Science, 1996. **31**(6): p. 1529-1535.

26. Zhang, J., et al., *Microstructural refinement in Al-Mg2Si in situ composites.* Journal of Materials Science Letters, 1999. **18**(10): p. 783-784.

27. Miller, W.S. and F.J. Humphreys, *Strengthening mechanisms in particulate metal matrix composites.* Scripta Metallurgica et Materialia, 1991. **25**(1): p. 33-38.

28. Li, C., et al., *Morphological evolution and growth mechanism of primary Mg2Si phase in Al–Mg2Si alloys.* Acta Materialia, 2011. **59**(3): p. 1058-1067.

29. Sunagawa, I., *Crystals: growth, morphology, and perfection*. 2005, Cambridge: Cambridge University Press.

30. Wang, R.Y., W.H. Lu, and L.M. Hogan, *Growth morphology of primary silicon in cast Al-Si alloys and the mechanism of concentric growth.* Journal of Crystal Growth, 1999. **207**(1-2): p. 43-54.

31. Lu, S.Z. and A. Hellawell, *The Mechanism of Silicon Modification in Aluminium-Silicon Alloys - Impurity Induced Twinning.* Metallurgical Transactions a-Physical Metallurgy and Materials Science, 1987. **18**(10): p. 1721-1733.

32. Srinivas, V. and V. Singh, *Development of In Situ As Cast Al-Mg2Si Particulate Composite: Microstructure Refinement and Modification Studies.* Transactions of the Indian Institute of Metals, 2012. **65**(6): p. 759-764.

33. Tebib, M., et al., *Effect of P and Sr additions on the microstructure of hypereutectic Al–15Si–14Mg–4Cu alloy.* Materials Characterization, 2014. **89**(0): p. 112-123.

34. Turnbull, D. and B. Vonnegut, *Nucleation Catalysis.* Industrial and Engineering Chemistry, 1952. **44**(6): p. 1292-1298.

35. Li, C., X.F. Liu, and G.H. Zhang, *Heterogeneous nucleating role of TiB2 or AlP/TiB2 coupled compounds on primary Mg2Si in Al-Mg-Si alloys.* Materials Science and Engineering a-Structural Materials Properties Microstructure and Processing, 2008. **497**(1-2): p. 432-437.

36. Li, C., X.F. Liu, and Y.Y. Wu, *Refinement and modification performance of Al-P master alloy on primary Mg2Si Al-Mg-Si alloys.* Journal of Alloys and Compounds, 2008. **465**(1-2): p. 145-150.

37. Zhang, Q., X. Liu, and H. Dai, *Re-formation of AlP compound in Al–Si melt.* Journal of Alloys and Compounds, 2009. **480**(2): p. 376-381.

38. Qin, J., et al., *The featured local structural units in liquid Al80Si15P5 alloy and their relationship with Si modification.* Journal of Alloys and Compounds, 2010. **492**(1–2): p. 525-528.

39. Liang, S.-M. and R. Schmid-Fetzer, *Thermodynamic assessment of the Al–P system based on original experimental data.* Calphad, 2013. **42**(0): p. 76-85.

40. Lescuyer, H., M. Allibert, and G. Laslaz, *Solubility and precipitation of AlP in Al-Si melts studied with a temperature controlled filtration technique.* Journal of Alloys and Compounds, 1998. **279**(2): p. 237-244.

41. Liang, S.-M. and R. Schmid-Fetzer, *Phosphorus in Al–Si cast alloys: Thermodynamic prediction of the AlP and eutectic (Si) solidification sequence validated by microstructure and nucleation undercooling data.* Acta Materialia, 2014. **72**(0): p. 41-56.

42. Wu, C.J., et al., *Experimental investigation and thermodynamic calculation of the Al-Fe-P system at low phosphorus contents.* Calphad-Computer Coupling of Phase Diagrams and Thermochemistry, 2012. **38**: p. 1-6.

43. Tu, H., et al., *Experimental investigation and thermodynamic modeling of the Al-P-Zn ternary system.* Calphad-Computer Coupling of Phase Diagrams and Thermochemistry, 2009. **33**(4): p. 755-760.

44. Ansara, I., et al., *A Binary Database for III-V Compound Semiconductor Systems.* Calphad-Computer Coupling of Phase Diagrams and Thermochemistry, 1994. **18**(2): p. 177-222.

45. Beer, S.Z., *Solution of Aluminium Phosphide in Aluminium.* Journal of the Electrochemical Society, 1969. **116**(2): p. 263-265.

46. Yeganeh, S.E.V., A. Razaghian, and M. Emamy, *The influence of Cu-15P master alloy on the microstructure and tensile properties of Al-25 wt% Mg2Si composite before and after hot-extrusion.* Materials Science and Engineering a-Structural Materials Properties Microstructure and Processing, 2013. **566**: p. 1-7.

47. Di Sabatino, M., et al., *Determination of relative sensitivity factors for trace element analysis of solar cell silicon by fast-flow glow discharge mass spectrometry.* Spectrochimica Acta Part B-Atomic Spectroscopy, 2011. **66**(2): p. 144-148.

48. Wang, C.C., M. Zaheeruddin, and L.H. Spinar, *Preparation and Properties of Aluminium Phosphide.* Journal of Inorganic & Nuclear Chemistry, 1963. **25**(3): p. 326-327.

49. Liao, J.N., et al., *Properties of Mg2Si (100) surfaces: A first-principles study.* Solid State Communications, 2014. **183**: p. 41-46.

50. Jian, Z.Y., et al., *Solid-Liquid Interface Energy between Silicon Crystal and Silicon-Aluminum Melt.* Metallurgical and Materials Transactions a-Physical Metallurgy and Materials Science, 2010. **41A**(7): p. 1826-1835.

51. Jian, Z.Y., K. Kuribayashi, and W.Q. Jie, *Solid-liquid interface energy of metals at melting point and undercooled state.* Materials Transactions, 2002. **43**(4): p. 721-726.

52. Smithells, C.J., T.C. Totemeier, and W.F. Gale, *Smithells metals reference book*. 2004, Amsterdam: Elsevier Butterworth-Heinemann.

53. Jackson, K.A., *Kinetics of Alloy Solidification.* Canadian Journal of Physics, 1958. **36**(6): p. 683-691.

54. Jackson, K.A., *On the theory of crystal growth: Growth of small crystals using periodic boundary conditions.* Journal of Crystal Growth, 1968. **3–4**(0): p. 507-517.

55. Bodak, O., et al., *Al-Mg-Si (Aluminium - Magnesium - Silicon)*, in *Light Metal Ternary Systems: Phase Diagrams, Crystallographic and Thermodynamic Data*, G. Effenberg and S. Ilyenko, Editors.

56. Moustafa, M.A., et al., *Effect of Mg and Cu additions on the microstructural characteristics and tensile properties of Sr-modified Al-Si eutectic alloys.* International Journal of Cast Metals Research, 2002. **14**(4): p. 235-253.

57. Eskin, D.G. and L. Katgerman, *Macrosegregation Mechanisms in Direct-Chill Casting of Aluminium Alloys*, in *Aluminium Cast House Technology Xi*, J.A. Taylor, J.F. Grandfield, and A. Prasad, Editors. 2010. p. 193-199.

58. Zhang, B.J., J.Z. Cui, and G.M. Lu, *Effect of low-frequency magnetic field on macrosegregation of continuous casting aluminum alloys.* Materials Letters, 2003. **57**(11): p. 1707-1711.

Appendix 1: Composition of standard samples for GDMS

Table 9: Composition of the five standard samples used for calculation of the relative sensitivity factors (RSFs). The phosphorous concentration of standard alloy 2007AA was not tabulated.

Standard alloy	^{24}Mg [wt%]	^{28}Si [wt%]	^{31}P [wt%]	^{44}Ca [wt%]	^{56}Fe [wt%]	^{63}Cu [wt%]
2011AC	0.0150	0.1200	0.0024	0.0009	0.2600	5.6200
7075AF	2.6600	0.1900	0.0010	0.0034	0.1700	1.7500
AA8112	0.0140	0.5200	0.0056	0.0025	0.6600	0.2600
5454AC	3.1600	0.2500	0.0013	0.0023	0.4000	0.1000
2007AA	0.5600	0.4600	-	0.0023	0.4100	4.2400

Appendix 2: Characteristic temperatures from thermal analysis

Table 10: Characteristic temperatures for the primary Mg_2Si reaction. The liquidus temperature for the nominal alloy composition is 628.0 °C.

P [ppm]	$T_{N,Mg2Si}$	$T_{min,Mg2Si}$	$T_{G,Mg2Si}$	$\Delta T_{R,Mg2Si}$
0	640.6 °C	632.4 °C	633.6 °C	1.2 °C
5	651.2 °C	644.9 °C	644.9 °C	0.0 °C
20	656.4 °C	652.9 °C	652.9 °C	0.0 °C
40	656.1 °C	652.8 °C	652.8 °C	0.0 °C
60	654.7 °C	651.7 °C	651.8 °C	0.1 °C
80	658.5 °C	655.2 °C	655.2 °C	0.0 °C
100	654.1 °C	650.4 °C	650.6 °C	0.2 °C
500	649.3 °C	645.9 °C	645.9 °C	0.0 °C

Table 11: Characteristic temperatures for the Al - Mg_2Si binary eutectic reaction. The equilibrium temperature for the Al-Mg_2Si binary eutectic reaction for the nominal alloy composition is 582.3 °C.

P [ppm]	$T_{N,Al-Mg2Si}$	$T_{min,Al-Mg2Si}$	$T_{G,Al-Mg2Si}$	$\Delta T_{R,Al-Mg2Si}$
0	587.2 °C	581.1 °C	583.9 °C	2.8 °C
5	584.6 °C	581.5 °C	584.1 °C	2.6 °C
20	584.5 °C	581.7 °C	584.1 °C	2.4 °C
40	584.4 °C	582.2 °C	583.9 °C	1.7 °C
60	583.8 °C	581.1 °C	583.3 °C	2.2 °C
80	585.4 °C	582.6 °C	584.2 °C	1.6 °C
100	584.0 °C	580.4 °C	583.2 °C	2.8 °C
500	584.1 °C	581.2 °C	582.3 °C	1.1 °C

Table 12: Characteristic temperatures for the Al - Mg_2Si - Si ternary eutectic reaction. The equilibrium temperature for the Al-Mg_2Si-Si ternary eutectic reaction is 557.0 °C.

P [ppm]	$T_{N,Al-Mg2Si-Si}$	$T_{min,Al-Mg2Si-Si}$	$T_{G,Al-Mg2Si-Si}$	$\Delta T_{R,Al-Mg2Si-Si}$
0	550.1 °C	547.4 °C	551.6 °C	4.2 °C
5	550.4 °C	547.4 °C	551.1 °C	3.7 °C
20	549.9 °C	547.6 °C	550.8 °C	3.2 °C
40	549.5 °C	547.1 °C	550.5 °C	3.4 °C
60	549.1 °C	547.1 °C	550.5 °C	3.4 °C
80	549.3 °C	547.1 °C	550.3 °C	3.2 °C
100	549.8 °C	547.3 °C	550.7 °C	3.4 °C
500	547.2 °C	544.7 °C	547.5 °C	2.8 °C

Appendix 3: Calculation of number of AlP particles in the melt

Table 13: Quantities used in the calculation with reference to where the values are found in the literature.

Quantity (Abbreviation)	Value [unit] [Reference]
Atomic weight of aluminium (M_{Al})	26.98 [g · mol^{-1}] [52, p. 3-1]
Atomic weight of phosphorous (M_P)	30.97 [g · mol^{-1}] [52, p. 3-1]
Density of aluminium phosphide (ρ_{AlP})	2.40 [g · cm^{-3}] [48]
Density of liquid aluminium ($\rho_{Al,L}$)	2.385 [g · cm^{-3}] [52, p. 14-10]
Density of liquid silicon ($\rho_{Si,L}$)	2.53 [g · cm^{-3}] [52, p. 14-10]
Density of liquid magnesium ($\rho_{Mg,L}$)	1.590 [g · cm^{-3}] [52, p. 14-10]

Assuming that the AlP particles are built up of Al_6P structural units, as described in the work of Qin et al. [38].

$$M_{Al_6P} = 192.86 \ g \cdot mol^{-1}$$

Assuming cubic particles, of mean diameter 5 µm as observed by the EPMA analysis. The assumption is reasonable as the observed AlP particles in the literature have a blocky structure [37].

$$m_{Particle} = \rho_{AlP} \cdot V_{Particle} = 3 \cdot 10^{-10} g \cdot particle^{-1}$$

We calculate the case for 100 g melt and 5 ppm P. 5 ppm P corresponds to 0.0005 g P in 100 g melt.

$$n_P = 1.6145 \cdot 10^{-5} mol \Rightarrow m_{AlP} = 3.1135 \cdot 10^{-3} g \ \text{AlP particles}$$

Dividing by the calculated mass of one AlP particle we get the number of AlP particles

$$n_{AlP} = m_{AlP} / m_{Particle} = 1.0378 \cdot 10^{7} \ particles$$

By the rule of mixtures we calculate the approximate melt density of the alloy.

$$\rho_{melt} = \rho_{Al,L} \cdot [wt\%Al] + \rho_{Si,L} \cdot [wt\%Si] + \rho_{Mg,L} \cdot [wt\%Mg] = 2.325 \ \ \text{g} \cdot \text{cm}^{-3}$$

For 100 g of melt this corresponds to a volume of

$$V_{melt} = 43.01 \ cm^3$$

This yields the number density of particles per unit volume for the alloy with 5 ppm P

$$ND_{AlP} = 2.413 \cdot 10^{5} \ particles \cdot cm^{-3} = 241 \ \ particles \cdot mm^{-3}$$

According to the recent work of Liang and Schmid-Fetzer the solubility of P in liquid aluminium is 34 ppm [41]. This would indicate that there should be no AlP particles precipitated for the alloys with 5 and 20 ppm P. This is unreasonable, as a significant decrease in the undercooling for the primary Mg_2Si reaction is observed, and the solubility is therefore not included in this calculation.